Electronic Supplementary Material (ESI) for Journal of Materials Chemistry A.

# Metal-Organic Frameworks to Satisfy Gas Upgrading Demands: Fine-tuning the soc-MOF platform for the Operative Removal of $H_2S$

Youssef Belmabkhout,*[a] Renjith S. Pillai,[b] Dalal Alezi,[a] Osama Shekhah,[a] Prashant M. Bhatt,[a] Zhijie Chen,[a] Karim Adil,[a] Sebastien Vaesen,[c] Guy. De Weireld,[c] Maolin Pan,[a] Mikhail Suetin,[a] Amy J. Cairns,[a] Vera Solovyeva,[a] Aleksander Shkurenko,[a] Omar El Tall,[d] Guillaume Maurin,[b] Mohamed Eddaoudi*[a]

## Table of contents

# 1. Materials and general procedures

## 1.1 Organic Synthesis

3,3’,5,5’-azabenzenetetracarboxylic acid (ABTC) was synthesized in our lab by recently published procedure (Scheme S1). Briefly, A mixture of 5-nitroisophthalic acid (19 g, 90 mmol) and NaOH (50 g, 1250 mmol) in 250 ml of reverse osmosis water was placed into a 1L 3-neck round bottom flask and stirred vigorously at 333 K. To this slurry 100 g of D-glucose dissolved in 150 ml of reverse osmosis water was slowly added. The resulted brown mixture was cooled down to room temperature and air was bubbled through reaction mixture overnight always under stirring. The reaction mixture was cooled with an ice bath and the sodium salt of 3,3’,5,5’-azobenzene tetracarboxylic acid was recovered by filtration and washed with small amount of cold water. The resulting yellow solid was then dissolved in 200 ml of reverse osmosis water and this solution was acidified to pH = 1 by the addition of conc. HCl. The resulting orange solid was collected by filtration on the fritted funnel, washed with reverse osmosis water and dried in vacuum oven at 373 K to provide 10.5 g of target compound. Yield 70 %. $^1$H and $^{13}$C NMR data are in a good agreement with previously reported data.[1]

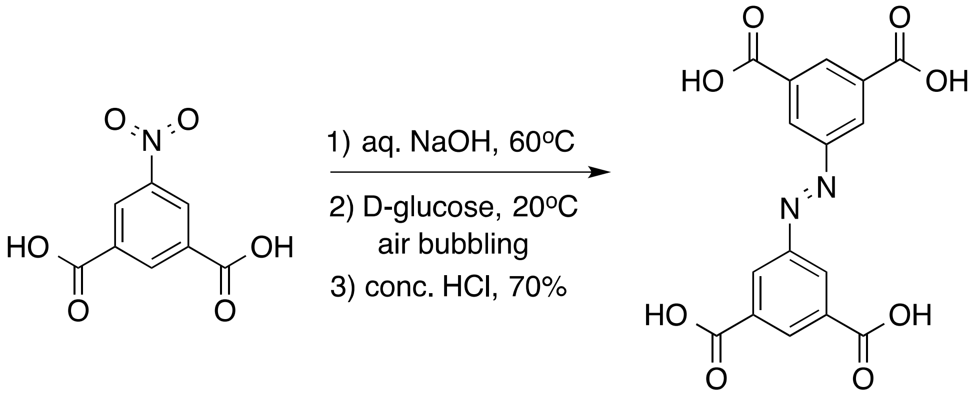

**Scheme S1:** Synthesis of 3,3’,5,5’-azobenzene tetracarboxylic acid (H4-ABTC)

All other chemicals and solvents were used as received unless otherwise stated from Fisher Scientific, Acros Organics, Sigma-Aldrich, Combi Blocks or TCI America. DMF was dried over $CaH_2$. DI water = deionized water. $^1$H and $^{13}$C NMR spectra were recorded at room temperature with Bruker Avance 500 and 600 MHz spectrometers using $CDCl_3$ or DMSO-$d_6$ as the solvents, and referenced to the corresponding solvent peaks (7.26 and 77.16 ppm for $CDCl_3$, and 2.50 and 39.52 ppm for DMSO- $d_6$, respectively).

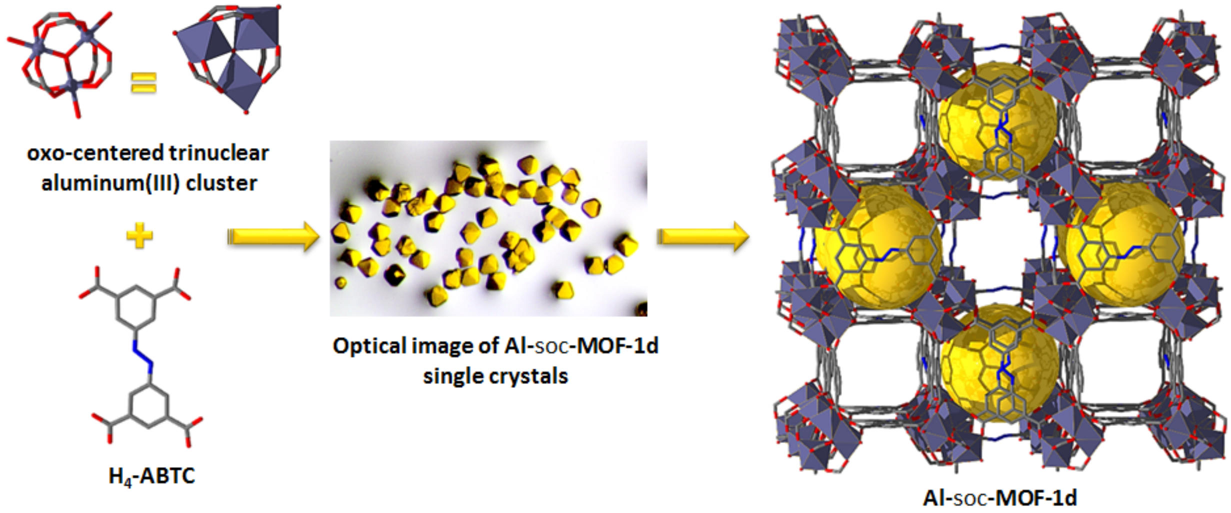

**Scheme S2:** Assembly of Al-**soc**-MOF-1d

## 1.2 Instrumentations and procedures

- **Single-crystal X-ray diffraction data:** Single-crystal X-ray diffraction data were collected using a Bruker X8 PROSPECTOR APEX2 CCD diffractometer (Cu Kα, λ = 1.54178 Å). Indexing was per-formed using APEX2 (Difference Vectors method).[2] Data integration and reduction were performed using SaintPlus 6.01.[3] Absorption correction was performed by multi-scan method implemented in SADABS.[4] Space groups were determined using XPREP implemented in APEX2.1 Structure was solved using SHELXS-97 (direct methods) and refined using SHELXL-97 (full-matrix least-squares on F2) contained in APEX2.[2]

- **Powder X-ray diffraction (PXRD)** measurements were carried out at room temperature on a PANalytical X'Pert PRO diffractometer 45 kV, 40 mA for Cu $K\alpha$ ($\lambda = 1.5418$ Å), with a step size of 0.05° in $2\theta$.

- **Quantachrome Low-pressure gas $N_2$ sorption measurements** were performed on a fully automated autosorb-1 high resolution gas adsorption analyzer (Quantachrome) at relative pressures up to 1 atm. The cryogenic temperatures were controlled using liquid nitrogen and argon baths at 77 K.

- **3FLEX Low-pressure gas sorption measurements at 298K**

  Low pressure gas adsorption measurements at 298 K were performed on 3-Flex Surface Characterization Analyzer (Micromeritics) at relative pressures up to 1 atm.

- **$C_4H_{10}/CH_4$ Column breakthrough test**

  The homemade set-up for adsorption column breakthrough testing is composed of a stainless steel column. The column is 27 mm in length with 4 mm of inner (6.4 mm outer) diameter. The gas composition downstream the column is monitored using a hidden mass spectrometer. In a typical experiment, 0.1–0.4 g of adsorbent was treated at 403-433 K overnight in vacuum (in oven). After backfill with argon, the column is then transferred to a thermostatic chamber where helium is flushed trough the column at 3.5 $cm^3$ $min^{-1}$. The gas flow is then switched to the desired n-$C_4H_{10}/CH_4$ (2/98) gas mixture at the same flow rate. The complete breakthrough of n-$C_4H_{10}$ and $CH_4$ were indicated by the downstream gas composition reaching that of the feed gas.

- **$H_2S/CO_2/CH_4$ Column breakthrough tests**

For $H_2S$ containing gases, the mixed gas testing measurements were carried out using custom made column breakthrough set-up, designed in collaboration with L&C (Hilleah, Florida USA). The stainless steel column used in the breakthrough test with a capacity of packing up to 2 g of materials. The column downstream is monitored using a MKS mass spectrometer. In a typical experiment, 0.1–0.4 g of adsorbent was treated at 403-433 K overnight in vacuum (in situ). The gas flow is then switched to the desired $CO_2/H_2S/CH_4$:5/5/90 gas mixture at the same flow rate (10 $cm^3$/min). The complete breakthrough of $CH_4$, $CO_2$ and $H_2S$ were indicated by the downstream gas composition reaching that of the feed gas.

- ***In-situ* FTIR**

Fourier Transform InfraRed (FTIR) spectra were measured using Thermo Nicolet 6700 series spectrometer equipped with quantum Mercuric Cadmium Telluride (MCT-A) detector operating at liquid nitrogen temperature. Each IR spectrum was the average of 128 spectra recorded in the 4000-650 $cm^{-1}$ spectral range with a resolution of 4 $cm^{-1}$.

Diffuse Reflectance Infrared Fourier Transform Spectroscopy (DRIFTS) experiments were performed using Praying Mantis module equipped with a dome sealed reaction chamber (ZnSe window) allowing a controlled in situ environment.

KBr powder was used to collect the background spectrum. Sample was mixed with KBr (1 wt%) for sample spectrum collection. KBr and KBr+sample powders were dried at 200$^o$C under ultrahigh vacuum (<1 mTorr) prior transferring to the reaction chamber in glovebox environment. Before measurement sample was heated at 200$^o$C under vacuum (1 torr) in the sealed reaction chamber.

- **TG-DSC**

Enthalpy of adsorption for $CO_2$ was measured using SENSYS evo TG-DSC from Setaram Instrumentation that can carry out simultaneous high resolution DSC and TGA experiments. In a typical experiment, the sample was activated in-situ 403-433 K under continuous dry $N_2$ flow at the rate of 15 ml/min. For sorption experiment, baseline was obtained under dry $N_2$ flow at the rate of 15ml/min at 25°C. The desired gas was connected at auxiliary gas port and gas was changed from $N_2$ to $CH_4$, $C_3H_8$ and n-$C_4H_{10}$ exactly after 1 hour and TGA and DSC signal were monitored for few hours to obtain uptake and heat of sorption respectively.

- **High-pressure gas sorption measurements**

Adsorption equilibrium measurements of pure gases were performed using a Rubotherm gravimetric-densimetric apparatus (Bochum, Germany) (Scheme S2), composed mainly of a magnetic suspension balance (MSB) and a network of valves, mass flow meters, and temperature and pressure sensors. The MSB overcomes the disadvantages of other commercially available gravimetric instruments by separating the sensitive microbalance from the sample and the measuring atmosphere, and is able to perform adsorption measurements across a wide pressure range (i.e., from 0 to 20 MPa). The adsorption temperature may also be controlled within the range of 77 K to 423 K. In a typical adsorption experiment, the adsorbent is precisely weighed and placed in a basket suspended by a permanent magnet through an electromagnet. The cell in which the basket is housed is then closed and vacuum or high pressure is applied. The gravimetric method allows the direct measurement of the reduced gas adsorbed amount (Ω). Correction for the buoyancy effect is required to determine the excess and absolute adsorbed amount using equations 1 and 2, where $V_{adsorbent}$ and Vss and $V_{adorbed}$ phase refer to the volume of the adsorbent, the volume of the suspension system, and the volume of the adsorbed phase, respectively.

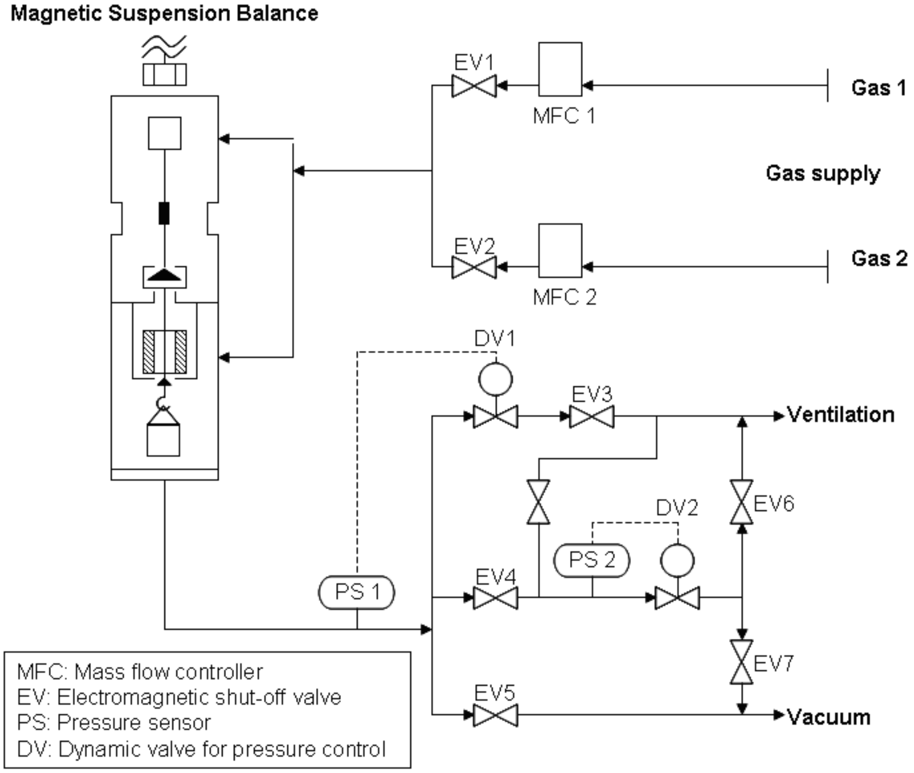

**Scheme S3:** Representation of the Rubotherm gravimetric-densimetric apparatus.

$$\Omega = m_{absolute} - \rho_{gas}(V_{adsorbent} + V_{ss} + V_{adsorbed-phase}) \quad (1)$$

$$\Omega = m_{excess} - \rho_{gas}(V_{adsorbent} + V_{ss}) \quad (2)$$

The buoyancy effect resulting from the adsorbed phase may be taken into account via correlation with the pore volume or with the theoretical density of the sample.

These volumes are determined using the helium isotherm method by assuming that helium penetrates in all open pores of the materials without being adsorbed. The density of the gas is determined using the Refprop equation of state (EOS) database and checked experimentally using a volume-calibrated titanium cylinder. By weighing this calibrated volume in the gas atmosphere, the local density of the gas is also determined. Simultaneous measurement of adsorption capacity and gas-phase density as a function of pressure and temperature is therefore possible.

The pressure is measured using two Drucks high pressure transmitters ranging from 0.5 to 34 bar and 1 to 200 bar, respectively, and one low pressure transmitter ranging from 0 to 1 bar. Prior to each adsorption experiment, about 200 mg of sample is outgassed at 473 K at a residual pressure of 10-6 mbar. The temperature during adsorption measurements is held constant by using a thermostat-controlled circulating fluid.

- **Prediction of multicomponent gas adsorption Ideal Adsorption Solution Theory (IAST)**

The Ideal Adsorption Solution Theory (IAST) proposed by Mayer and Prausnitz (1965) uses pure gas adsorption isotherms to predict the mixture adsorption equilibrium at the temperature of interest. For IAST application, the main condition to be fulfilled is the availability of (i) good quality single component adsorption data of different gases, and (ii) an excellent curve fitting model for such data. In the current work, MSL and DSL models were used to fit the pure gas isotherms, as mentioned earlier

The most important equations used in the IAST calculation are listed hereafter:

$$f_i = x_i f_i^0(\pi) \tag{3}$$

$$\frac{\pi A}{RT} = \int_0^{f_i^0} n_i d \ln f_i \tag{4}$$

$$\frac{1}{n_t} = \sum_i \frac{x_i}{n_i^0} \tag{5}$$

$$S_{CO_2-i} = \frac{x_{CO_2} / x_i}{y_{CO_2} / y_i} \tag{6}$$

where $f_i$ is the fugacity of component i in the gas phase; $f_i^0$ is the standard-state fugacity (i.e., the fugacity of pure component *i* at the equilibrium spreading pressure of the mixture, $\pi$); $x_i$ and $y_i$ are the mole fractions of component i in the adsorbed and gas phase, respectively; $A$ is the surface area of the adsorbent; $n_i$ is the number of moles adsorbed of pure component *i* (i.e., the pure-component isotherm); and $n_i^0$ is the number of moles adsorbed of pure component *i* at the standard-state pressure.

Equation 3 is the central equation of IAST, specifying the equality of the chemical potential of component *i* in the gas and the adsorbed phase (which is assumed to be ideal in the sense of Raoult's law). Equation 4 allows the calculation of the spreading pressure from the pure-component adsorption isotherm. The total amount adsorbed of the mixture, $n_t$, and the selectivity of $CO_2$ with respect to *i*, $S_{CO_2-i}$, are given by equations 5 and 6, respectively. The selectivity, $S_{CO_2-i}$, reflects the efficiency of $CO_2$ separation.

## 1.3 General information

**Table S1**: Typical composition of refinery-off gas (ROG)

| Components of ROG | Typical ROG Composition |
|---|---|
| $H_2$ | ~5-35 % |
| CO | 0.1-0.5 % |
| $N_2$ | 3-10 % |
| $CO_2$ | 0.1-0.5 % |
| $CH_4$ | 30-50 % |
| $C_2H_2$ | 1-15 ppm (vol) |
| Ethylene | 5-20 % |
| Ethane | 15-25% |
| Methyl acetylene & propadiene | 60-80 ppm (vol) |
| Propane | 1-5% |
| Propylene | 1-5% |
| Butadiene | 0-0.1 |
| Butylene | 0.1-0.3 |
| Butanes | 0.5-1 |
| $C_{5+}$ | 0.2-1.5 |

**Table S2:** Typical composition of natural gas

| Natural Gas Components | Typical Raw Natural Gas Composition | Natural Gas Pipeline Specifications |
|---|---|---|
| $CH_4$ | ~70-90 % | > 96% |
| $CO_2$ | Up to 10% | < 2% |
| Total inerts ($N_2$, $CO_2$) | Up to 50% | < 4% |
| $H_2S$ | Up to 20% | < 4 ppm |
| $H_2O$ | Saturated | < 120 ppm |
| $C_{2+}$ hydrocarbons | Up to 20% | 950-1,050 Btu/scf<br>Dew point < -20°C |

**Table S3**: Polarizability of major common gases contained in NG and ROG[5]

| Gas | Polarizability × $10^{25}$ /$cm^3$ |
|---|---|
| $H_2$ | 08.00 |
| $N_2$ | 17.40 |
| $O_2$ | 15.80 |
| $CH_4$ | 25.93 |
| $C_2H_6$ | 44.50 |
| $C_2H_4$ | 42.50 |
| $C_3H_8$ | 64.00 |
| $C_3H_6$ | 62.60 |
| n-$C_4H_{10}$ | 82.00 |

## 2. Crystallographic data

Crystal data and refinement conditions of Al-**soc**-MOF-1d are shown in Table S4.

**Table S4**: Crystal data and structure refinement for Al-**soc**-MOF-1d

| | |
|---|---|
| Identification code | Al-**soc**-MOF-1d |
| Empirical formula | $C_{24}H_{17}Al_3N_3O_{17.5}$ |
| Formula weight | 708.34 |
| Crystal system, space group | Cubic, $P\bar{4}3n$ |
| Unit cell dimensions | $a$ = 21.4934(5) Å |
| Volume | 9929.2(7) Å$^3$ |
| $Z$, calculated density | 8, 0.948 Mg m$^{-3}$ |
| $F$(000) | 2888 |
| Temperature (K) | 100.0(1) |
| Radiation type | Cu $K\alpha$ |
| Absorption coefficient | 1.18 mm$^{-1}$ |
| Absorption correction | Multi-scan |
| Max and min transmission | 0.653 and 0.753 |
| Crystal size | 0.01 × 0.02 × 0.02 mm |
| Shape, color | Square pyramid, yellow |
| $\theta$ range for data collection | 5.0–66.5° |
| Limiting indices | $-22 \leq h \leq 21$, $-25 \leq k \leq 24$, $-25 \leq l \leq 23$ |
| Reflection collected / unique / observed with $I > 2\sigma(I)$ | 34324 / 2916 ($R_{\text{int}}$ = 0.041) / 2806 |
| Completeness to $\theta_{\text{max}}$ = 40.0° | 99.3 % |
| Refinement method | Full-matrix least-squares on $F^2$ |
| Data / restraints / parameters | 2916 / 3 / 154 |
| Final $R$ indices [$I > 2\sigma(I)$] | $R_1$ = 0.033, $wR_2$ = 0.089 |
| Final $R$ indices (all data) | $R_1$ = 0.034, $wR_2$ = 0.090 |
| Weighting *scheme* | $[\sigma^2(F_o^2) + (0.0644P)^2 + 1.4289P]^{-1*}$ |
| Goodness-of-fit | 1.02 |
| Largest diff. peak and hole | 0.32 and -0.25 e Å$^{-3}$ |

$^*P = (F_o^2 + 2F_c^2)/3$

## 3. Gas adsorption data

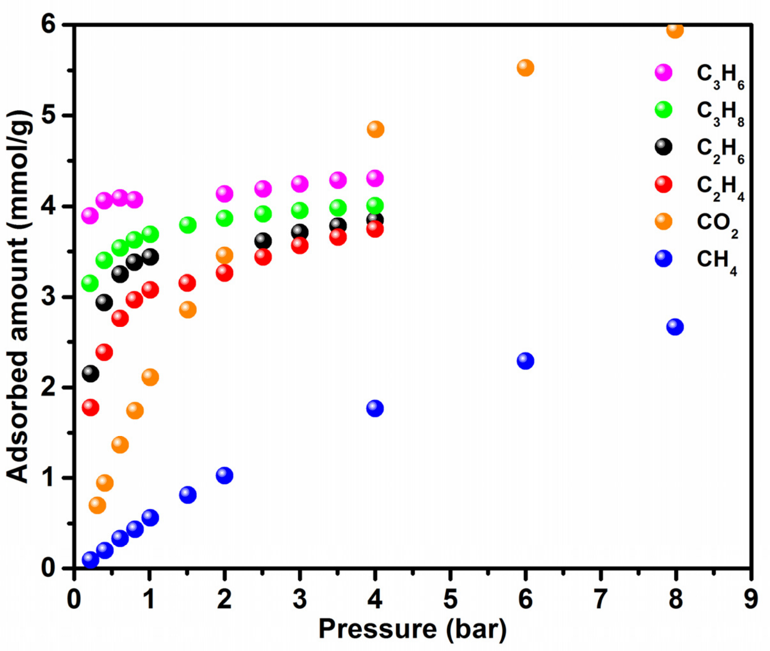

**Figure S1**: Adsorption of $N_2$, $CH_4$, $CO_2$, $C_2H_6$, $C_2H_6$, $C_3H_8$ and $C_3H_6$ on In-**soc**-MOF-1a at 298 K

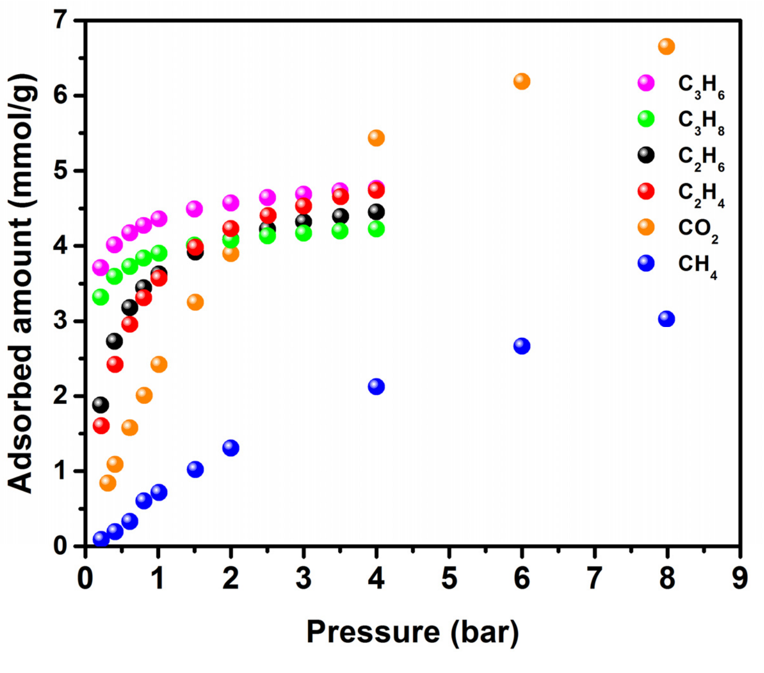

**Figure S2**: Adsorption of $CH_4$, $CO_2$, $C_2H_6$, $C_2H_6$, $C_3H_8$ and $C_3H_6$ on In-**soc**-MOF-1b at 298 K

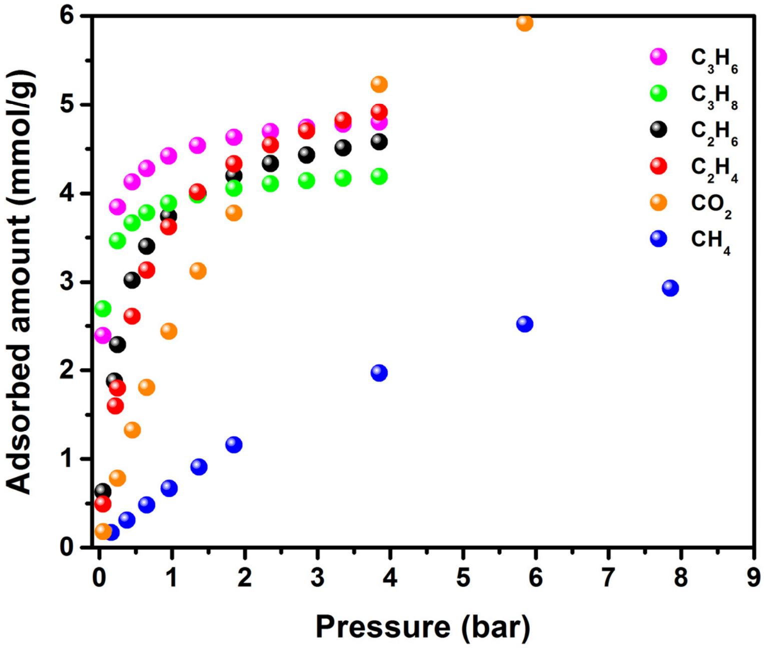

**Figure S3**: Adsorption of $CH_4$, $CO_2$, $C_2H_6$, $C_2H_6$, $C_3H_8$ and $C_3H_6$ on In-**soc**-MOF-1c at 298 K

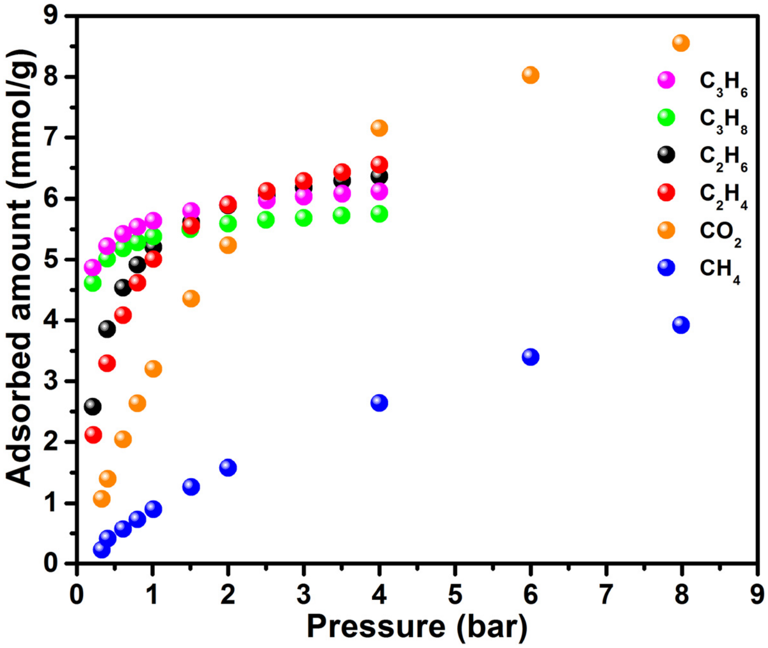

**Figure S4**: Adsorption of $CH_4$, $CO_2$, $C_2H_6$, $C_2H_6$, $C_3H_8$ and $C_3H_6$ on Fe-**soc**-MOF-1a at 298 K

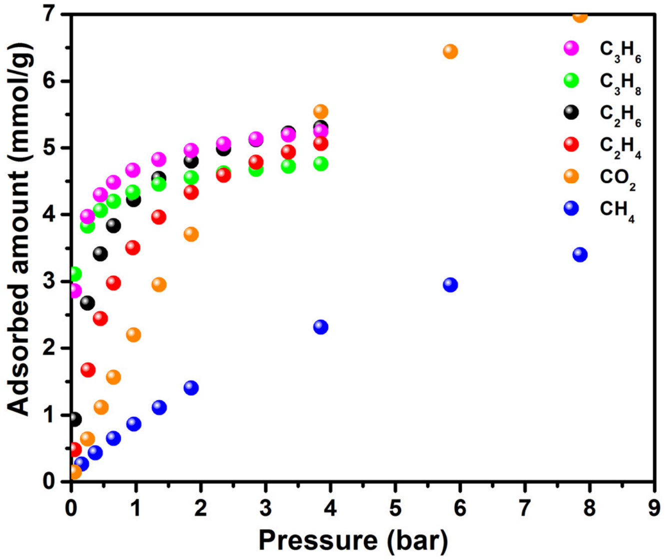

**Figure S5**: Adsorption of $CH_4$, $CO_2$, $C_2H_6$, $C_2H_6$, $C_3H_8$ and $C_3H_6$ on Ga-**soc**-MOF-1a at 298 K.

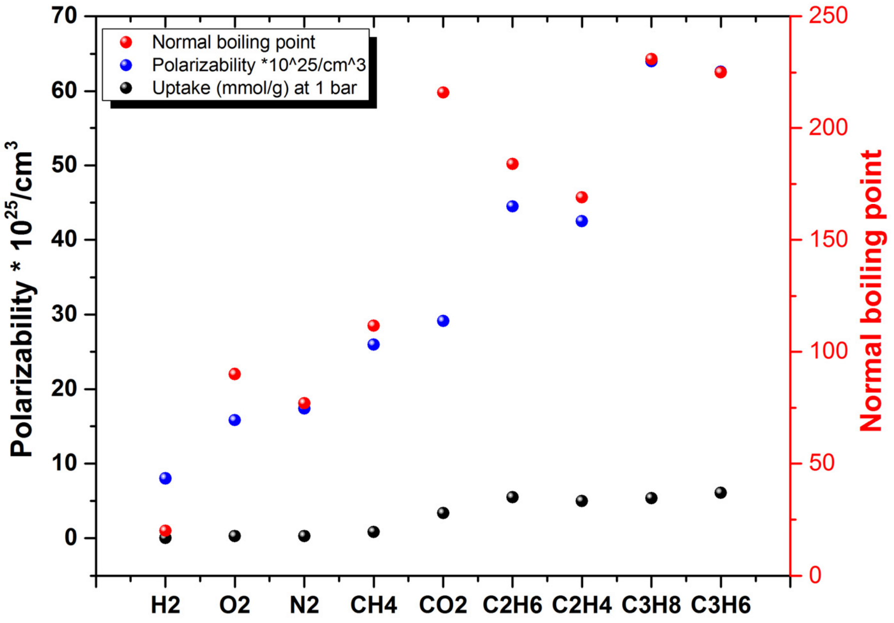

**Figure S6**: Adsorption uptake as a function of probe molecules normal boiling point and polarizabilities for Fe-**soc**-MOF-1b.

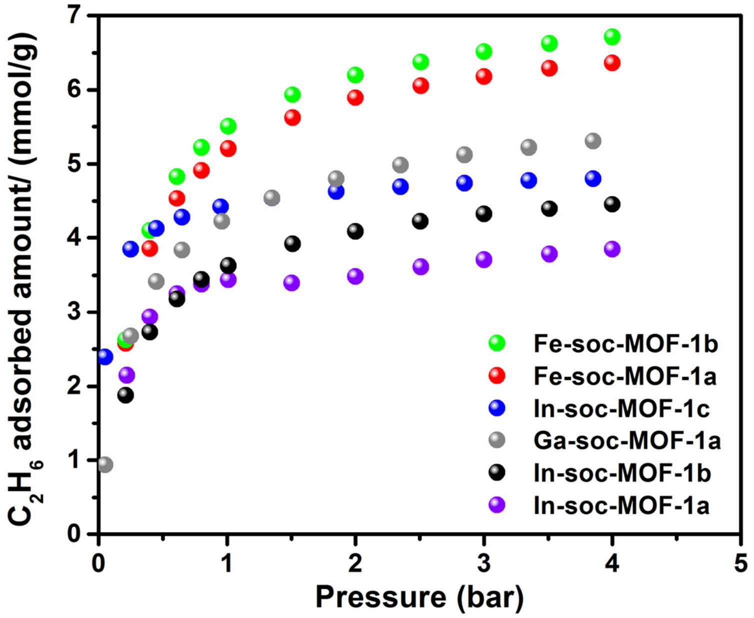

**Figure S7**: $C_2H_6$ adsorption isotherms on all of **soc**-MOF analogues at 298 K.

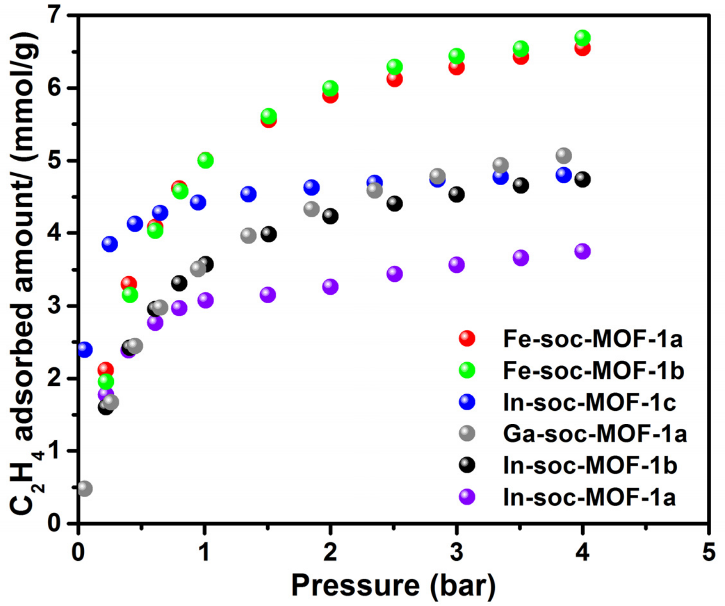

**Figure S8**: $C_2H_4$ adsorption isotherms on all of **soc**-MOF analogues at 298 K.

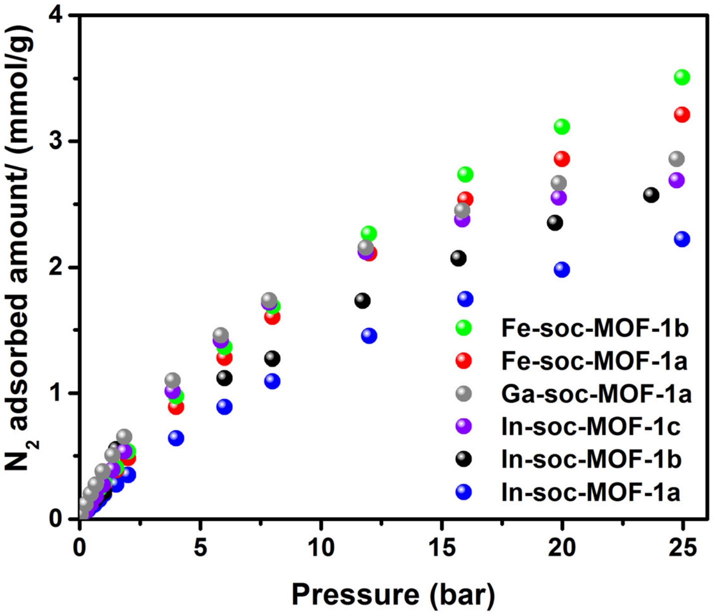

**Figure S9**: $N_2$ adsorption isotherms on all of **soc**-MOF analogues at 298 K.

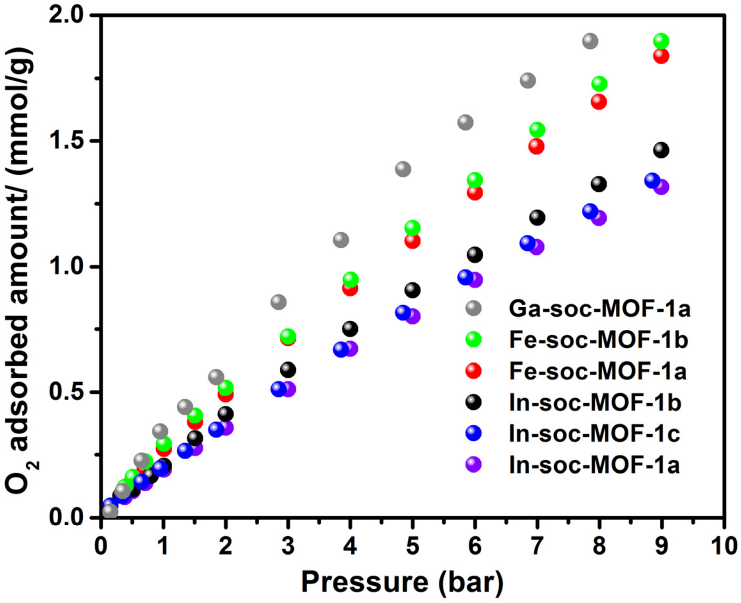

**Figure S10**: $O_2$ adsorption isotherms on all of **soc**-MOF analogues at 298 K.

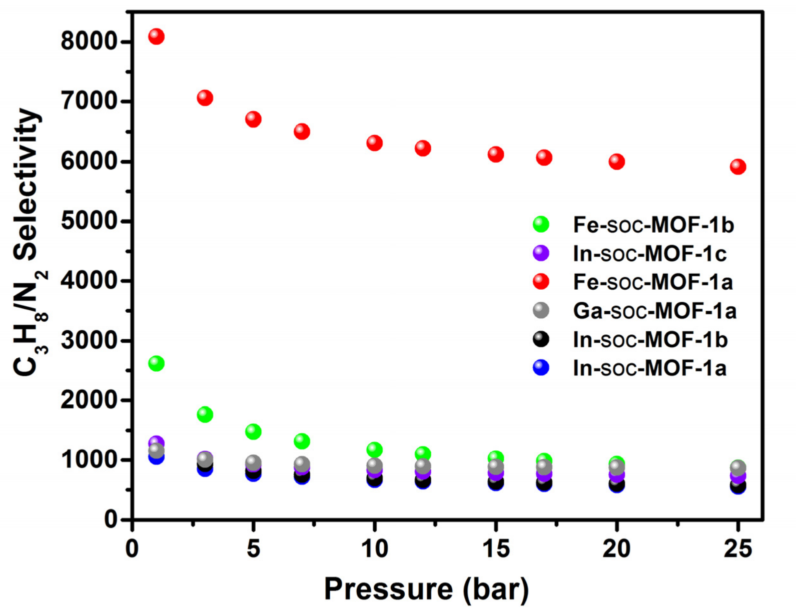

**Figure S11**: $C_3H_8/N_2$ selectivity for all **soc**-MOFs as determined using IAST combined with Toth Model

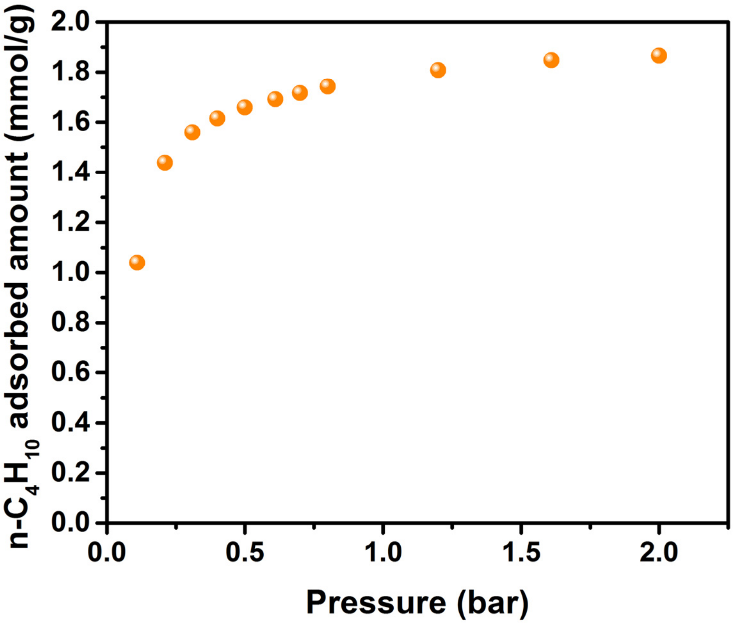

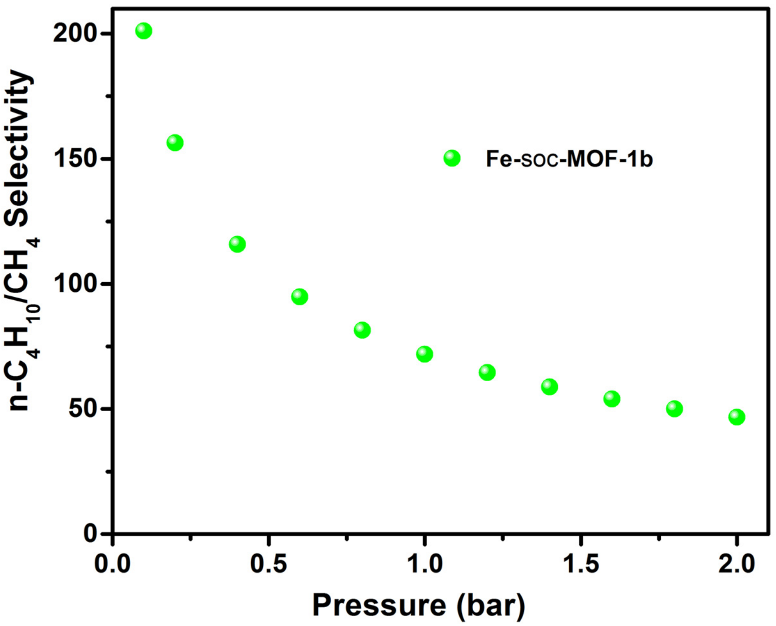

**Figure S12**: top) *n*-$C_4H_{10}$ adsorption isotherm and (botom) *n*-$C_4H_{10}$/$CH_4$ selectivity for Fe-**soc**-MOF-1b as determined using IAST combined with Toth Model

**Table S5**: Toth parameters for adsorption on **soc**-MOF analogues.

| | Parameters | Gases | | | | | |
|---|---|---|---|---|---|---|---|
| | | **$CH_4$** | **$C_2H_6$** | **$C_3H_8$** | **n-$C_4H_{10}$** | **$CO_2$** | **$N_2$** |
| In-**soc**-MOF-1a | $n_s$ | 5.4 | 4.04 | 4.2 | - | 8.23 | 5.2 |
| | **K*** | **0.107** | **5.7** | **77.7** | **-** | **0.32** | **0.03** |
| | m | 1.06 | 1.01 | 0.59 | - | 1.04 | 0.82 |
| In-**soc**-MOF-1b | $n_s$ | 5.9 | 4.77 | 4.7 | - | 9.14 | 4.99 |
| | **K*** | **0.12** | **3.23** | **393** | **-** | **0.32** | **0.04** |
| | m | 1.03 | 0.99 | 0.42 | - | 1.05 | 1.05 |
| In-**soc**-MOF-1c | $n_s$ | 5.49 | 5.04 | 4.63 | - | 8.25 | 4.7 |
| | **K*** | **0.13** | **0.43** | **599** | **-** | **0.43** | **0.08** |
| | m | 1.04 | 1 | 0.41 | - | 1 | 0.79 |
| Fe-**soc**-MOF-1a | $n_s$ | 7.65 | 7.01 | 6.13 | - | 11.64 | 6.35 |
| | **K*** | **0.12** | **2.84** | **1716** | **-** | **0.34** | **0.043** |
| | m | 1.02 | 1.01 | 0.52 | - | 1.06 | 0.967 |
| Fe-**soc**-MOF-1b | $n_s$ | 8.33 | 7.54 | 6.52 | 2 | 12.5 | 8.43 |
| | **K*** | **0.102** | **2.61** | **1957** | **193** | **0.33** | **0.03** |
| | m | 1.06 | 0.35 | 0.35 | 0.55 | 1.06 | 0.84 |
| Ga-**soc**-MOF-1a | $n_s$ | 6.04 | 5.99 | 5 | 3.99 | 8.8621 | 4.71 |
| | **K*** | **0.12** | **4.58** | **315** | **3600** | **0.308** | **0.09** |
| | m | 1.003 | 0.78 | 0.47 | 0.33 | 1.24 | 0.8 |
| Al-**soc**-MOF-1d | $n_s$ | 8 | 6.34 | 5.7 | 4.89 | - | - |
| | **K*** | **0.14** | **3.37** | **80.4** | **1116** | **-** | **-** |
| | m | 0.92 | 1.21 | 0.77 | 0.61 | - | - |

*parameter K has direct relation to the heat of adsorption

# 4. DFT and GCMC calculations

Cluster model calculations were carried out based on first principles density functional theory (DFT) calculations at the M062x/6-311G level of theory[6] as implemented in Gaussian. These simulations aimed to evaluate the binding energy of the guests on the Ga(III) sites and to evaluate the potential energy curve for further derivation of the force field parameters to represent the guest/Ga(III) sites interactions. Grand canonical Monte Carlo (GCMC) simulations were performed to determine the single component adsorption isotherms and enthalpies for $CH_4$ and *n*-$C_4H_{10}$ at 298 K up to 1 bar in Ga-**soc**-MOF-1a and the selectivity for the binary mixture Analysis of the Monte Carlo configurations was undertaken to carefully characterize the adsorption and co-adsorption mechanisms in play. All details of these calculations are described in Supplementary.

## 4.1. Interaction energy profile for the CUS-Ga /guests

Gaussian quantum chemistry program package[7] has been employed to first geometry optimize at the DFT level the adduct formed by both $CH_4$ and *n*-$C_4H_{10}$ and a cluster cut from the periodic structure of Ga-**soc**-MOF-1a. The corresponding geometry optimized alkane-loaded clusters built by a trimer of Ga-CUS containing the $NO_3$ as counter-anion and 1 guest molecule are reported in Figure S13. The DFT calculations have been performed at the M062x/6-311G level of theory[6].

The binding energies were further calculated as follows: $E_{B.E.}$ = E (Cluster +guest) – {E(Cluster) + E (guest)}, where E(Cluster + guest) corresponds to the energy of the optimized guest-loaded cluster while E(Cluster) and E(guest) are the total energies of the MC model and molecule taken individually. Binding energies were corrected for the basis set superposition error (BSSE).

A series of binding energy calculations has been performed for revealing potential energy curve of interaction in a system: gas molecule --- MOFs' cluster. The energy minimum has been obtained from the simulations of geometry optimization of the system gas molecule --- MOFs' cluster. The series of coordinates for binding energy simulation is situated on line, which started from the copper metal of

MOFs' cluster and pass through the energy minimum coordinate obtained earlier, as shown in Figure S13. The distance between the nearest binding energy calculations (step) is 0.1 Å.

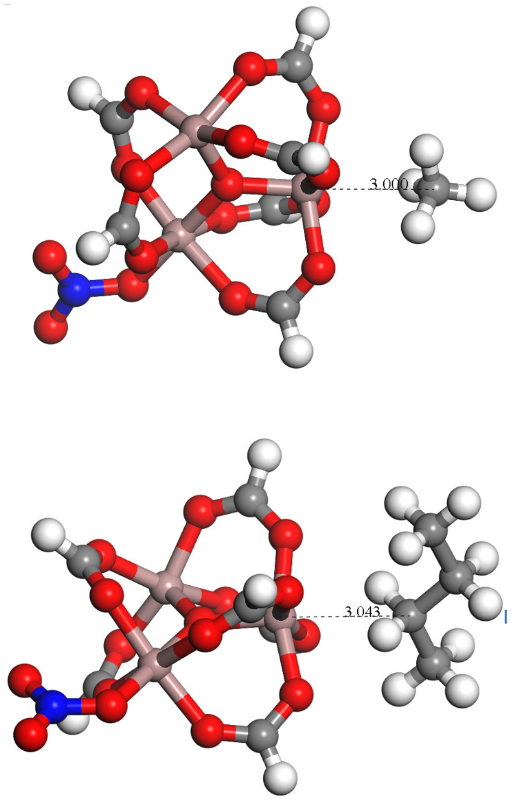

**Figure S13.** DFT geometry optimization of (i) the $CH_4$-Ga-**soc**-MOF-1a cluster (a) and the $n$-$C_4H_{10}$-Ga-**soc**-MOF-1a cluster (b). The arrow indicates the considered direction considered to displace step-wise the guest from the cluster. The color code is the same as defined in Figure S1.

## 4.2. Interatomic Potential parameters.

The interactions between Ga-**soc**-MOF-1a framework and the guest species were treated with van der Waals contribution only, although two different analytical functions have been employed for the van der Waals term:

(1) the interactions between the adsorbate species ($CH_4$ and *n*-$C_4H_{10}$) and all atoms of the MOF framework except the CUS-Ga were treated by using the standard 12-6 Lennard-Jones (LJ) potential (equation 1). The universal force field (UFF)[8] and DREIDING[9] parameters were considered to describe the LJ potential parameters for the atoms of the inorganic and organic nodes of Ga-**soc**-MOF-1a respectively (Table S6). Neutral United Atom (UA) models were considered for both $CH_4$ and *n*-$C_4H_{10}$ with LJ potential parameters taken from the TraPPE forcefield (Table S7)[10]. The LJ interacting sites are denoted as $CH_4\_sp^3$ for $CH_4$, similarly as $CH_3\_sp^3$ and $CH_2\_sp^3$ for –$CH_3$ and –$CH_2$- centers of *n*-$C_4H_{10}$, respectively.

$$U_{ij} = \underbrace{4\varepsilon_{ij}\left[\left(\frac{\sigma_{ij}}{r_{ij}}\right)^{12} - \left(\frac{\sigma_{ij}}{r_{ij}}\right)^{6}\right]}_{\text{Lennard-Jones term}} \qquad (1)$$

Here, $r_{ij} = |r_i - r_j|$ accounts for the distance between centers *i* and *j*, $\varepsilon_{ij}$ and $\sigma_{ij}$ are the LJ parameters between such sites. Interactions between unlike force field centers *i* and *j* were treated by means of the Lorentz-Berthelot (LB) combination rules ($\varepsilon_{ij} = \sqrt{\varepsilon_i \varepsilon_j}$ , $\sigma_{ij} = (\sigma_i + \sigma_j)/2$ , where $\varepsilon_i$ and $\varepsilon_j$, $\sigma_i\ and\ \sigma_j$ are the LJ parameters for the species *i* and j respectively.

(2) the interactions between the guest molecules and the CUS-Ga were described by a Buckingham potential, where equation 2 and 3 were considered for $CH_4$ and *n*-$C_4H_{10}$ , respectively.

$$U_{ij} = \underbrace{\left[A_{CH_4\_sp3_{ij}} e^{-B_{CH_4\_sp3_{ij}} r_{ij}}\right]}_{\text{Buckingham term}} \qquad (2)$$

$$U_{ij} = \underbrace{\left[A_{CH_3\_sp3_{ij}} e^{-B_{CH_3\_sp3_{ij}} r_{ij}} + A_{CH_2\_sp3_{ij}} e^{-B_{CH_2\_sp3_{ij}} r_{ij}} - S_g \frac{C_{ij}}{r_{ij}^6}\right]}_{\text{Buckingham term}} \qquad (3)$$

where $A_{CH_4\_sp3_{ij}}$, $A_{CH_3\_sp3_{ij}}$, $A_{CH_2\_sp3_{ij}}$ $B_{CH_4\_sp3_{ij}}$, $B_{CH_3\_sp3_{ij}}$, $B_{CH_2\_sp3_{ij}}$, and $C_{ij}$ are the conventional Buckingham parameters for repulsive and attractive contribution, respectively and $S_g$ is the global scaling factor for the dispersion energies. This choice of potential was based on previous work[11] which stated that such a specific Metal-cus sites/guest interaction is much better described by a Buckingham profile. These Buckingham potential parameters for both $CH_4$/ CUS-Ga and *n*-$C_4H_{10}$/ CUS-Ga pairs were extracted from the DFT-derived energy profile on the clusters represented in Figure S14 as detailed below.

### 4.3. Force field parameterization for CUS-Ga /guests

Following the same strategy previously reported[11] for other CUS-containing MOFs, the DFT-computed energy ($E_{DFT}$) profile for the cluster/$CH_4$ was decomposed into short-range exchange repulsion and dispersion interactions. The $CH_4$-CUS Ga interaction energy ($E_{CH_4-Ga}$) profile was thus obtained by subtracting from $E_{DFT}$ the 12-6 LJ contributions between $CH_4$ and the rest of the atoms of the cluster ($E_{LJ}$), i.e $E_{CH_4-Ga} = E_{DFT}$ - $E_{LJ}$ ,The dispersion term of ($E_{dispCH_4-Ga}$) was first computed using a C dispersion coefficient in the same range of value than that commonly considered in force fields[11] for CUS-containing MOFs. It is known that that these coefficients cannot lead to reasonable absolute energies. To correct this, we introduced a global scaling factor, $S_g$ in such a way to ensure that the short-range repulsion term ($E_{repulsionCH_4-Ga}$), obtained by $E_{repulsionCH_4-Ga}$ =$E_{CH_4-Ga}$ - $E_{dispCH_4-Ga}$ is positive in the whole range of the explored path. The $E_{repulsionCH_4-Ga}$ was then fitted in equation 2 to determine the pairwise repulsive parameters $A_{CH_4\_sp3_{ij}}$ and $B_{CH_4\_sp3_{ij}}$. The fitting can be further fine-tuned to obtain the optimal set of $A_{CH_4\_sp3_{ij}}$, $B_{CH_4\_sp3_{ij}}$ and $C_{ij}$ parameters by minimizing the error, e.g., difference between the energies computed by the force field and by DFT along the energy path. As a typical illustration on $CH_4$. Table S8 reports the corresponding set of Buckingham parameters and Figure S14 shows the comparison of the energy profile for the clusters calculated by the derived force-field and by the DFT calculations.

The same methodology was further employed for the $n$-$C_4H_{10}$ by considering equation 3 to fit the DFT energy profile in order to determine simultaneously the pairwise repulsive parameters $A_{CH_3\_sp3_{ij}}$, $A_{CH_2\_sp3_{ij}}$ $B_{CH_3\_sp3_{ij}}$, and $B_{CH_2\_sp3_{ij}}$. Similarly Figure S15 shows the comparison of the energy profile for the clusters calculated by the derived force-field and by the DFT calculations for $n$-$C_4H_{10}$. Indeed both Figures indicate a rather good agreement between the DFT- and the force-field based-calculations.

**Table S6.** LJ potential parameters for the atoms of Ga-**soc**-MOF-1a.

| **Atomic type** | **LJ potential** | |
|---|---|---|
| | **σ (Å)** | **ε/k$_B$ (K)** |
| C | 3.473 | 47.857 |
| H | 2.846 | 7.649 |
| N | 3.661 | 38.975 |
| O | 3.118 | 30.195 |
| Ga | 3.904 | 208.837 |

**Table S7.** Potential parameters for the alkanes.

| **Atomic type** | **σ (Å)** | **ε/k$_B$ (K)** |
|---|---|---|
| $CH_4\_sp^3$ | 3.730 | 148.000 |
| $CH_3\_sp^3$ | 3.750 | 98.000 |
| $CH_2\_sp^2$ | 3.950 | 46.000 |

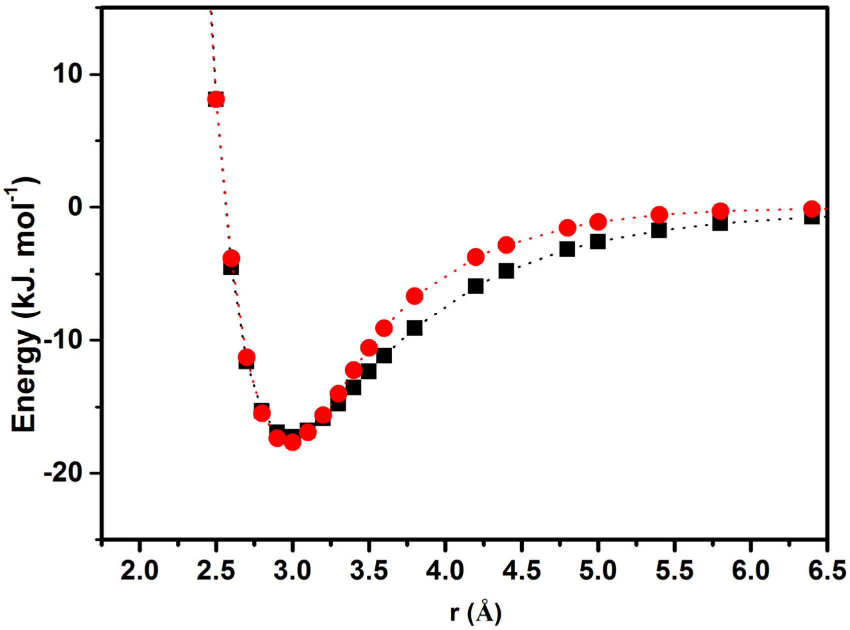

**Figure S14.** Comparison between the $CH_4$-framework interaction energy profile as a function of the separating distance between the CUS and $CH_4$ obtained by DFT calculations (red circle) and by force field based molecular simulations (black squares) along the $CH_4$-Ga pathway as defined in Figure S13.

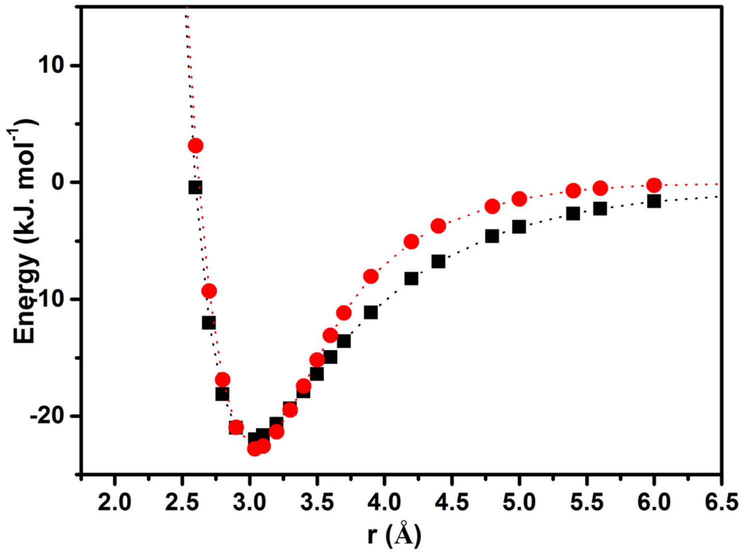

**Figure S15.** Comparison between the $nC_4H_{10}$-framework interaction energy profiles represented as a function of the separating distance between the CUS and $C_4H_{10}$ obtained by DFT calculations (red circle) and by force field based molecular simulations (black squares) along the $nC_4H_{10}$-Ga pathway as defined in Figure S13.

**Table S8.** Derived force-field parameters for the interactions between the two guest molecules and CUS-Ga. Three parameters (***Aij***, ***Bij***, ***Cij***) with the units of (K, Å$^{-1}$, KÅ$^{6}$) are displayed while the Buckingham potential is adopted.

| **Adsorbate** | ***Aij* (K)** | *Bij* **(Å$^{-1}$)** | *Cij* **(KÅ$^{6}$)** |
|---|---|---|---|
| $CH_4$_sp$^3$ | 6.87E+08 | 5.01 | 232000.0 |
| $CH_3$_sp$^3$ | 5.05E+08 | 5.00 | 232000.0 |
| $CH_2$_sp$^2$ | 4.81E+08 | 5.20 | 232000.0 |

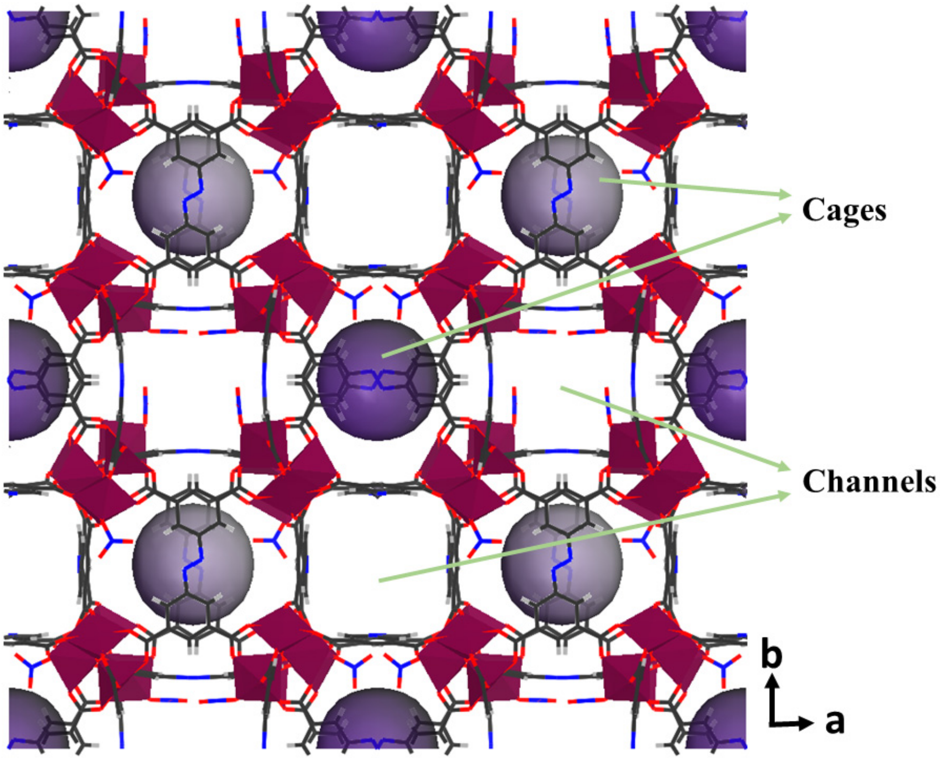

**Figure S16:** Illustration of the inaccessible cages of Ga-**soc**-MOF-1a for *n*-$C_4H_{10}$ due to steric limitation induced by windows of smaller size than the kinetic diameter of this alkane molecule. (Color code: Ga, brown; C, dark gray; O, red; N, blue; H, light gray).

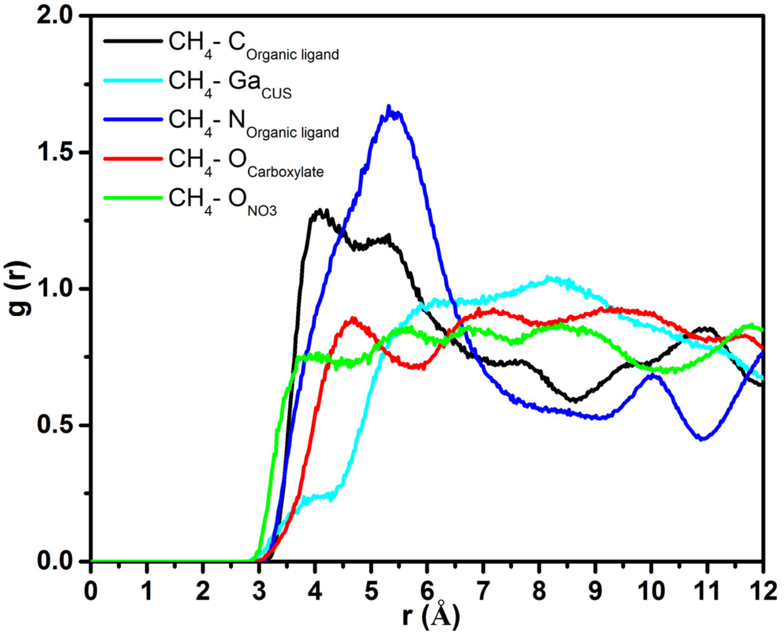

**Figure S17.** Radial distribution functions between $CH_4$ and the atoms of the MOF framework (organic linker carbon, $C_{Organic\ Linker}$: black, carboxylate oxygen, $O_{Carboxylate}$: red, organic linker nitrogen, $N_{Organic\ Linker}$: blue, nitrate oxygen, $O_{NO3}$: green and CUS Gallium $Ga_{CUS}$: cyan) extracted from the single component adsorption in Ga-**soc**-MOF-1a at 0.1 bar and 298 K.

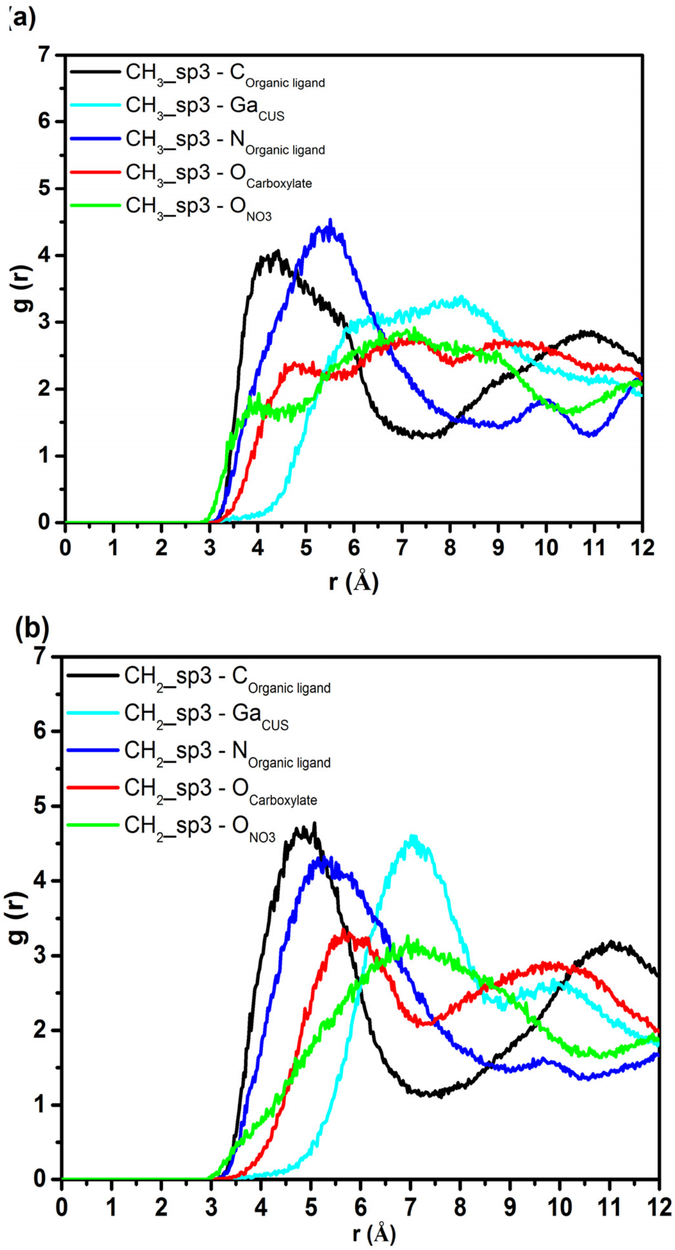

**Figure S18.** Radial distribution functions between *n*-$C_4H_{10}$ and the atoms of the MOF framework: -$CH_3$ (a) and -$CH_2$- (b) centers (organic linker carbon, $C_{\text{Organic Linker}}$: black, carboxylate oxygen, $O_{\text{Carboxylate}}$: red, organic linker nitrogen, $N_{\text{Organic Linker}}$: blue, nitrate oxygen, $O_{\text{NO3}}$: green and CUS Gallium $Ga_{\text{CUS}}$: cyan) extracted from the single component adsorption in Ga-**soc**-MOF-1a at 0.01 bar and 298 K.

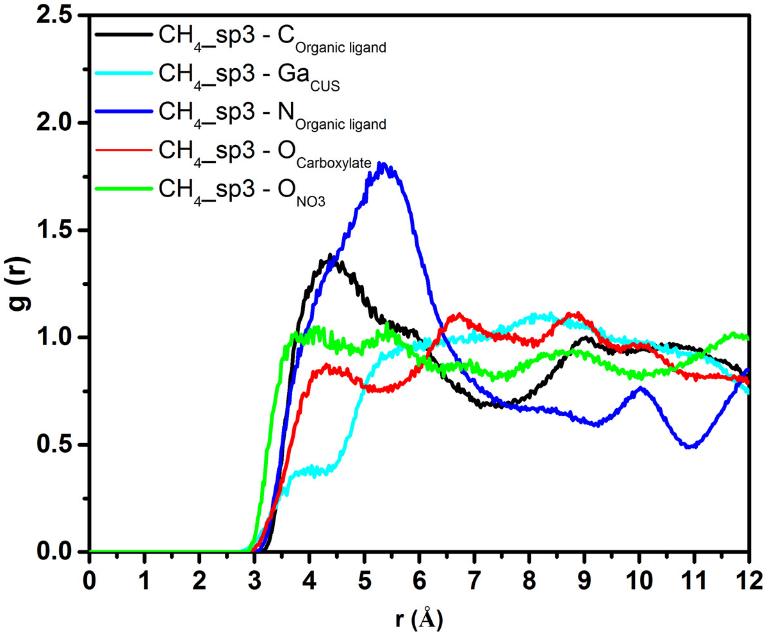
2.5
2.0
1.5
1.0
0.5
0.0
g (r)
0 1 2 3 4 5 6 7 8 9 10 11 12
r (Å)
CH$_4$_sp3 - C$_{Organic\ ligand}$
CH$_4$_sp3 - Ga$_{CUS}$
CH$_4$_sp3 - N$_{Organic\ ligand}$
CH$_4$_sp3 - O$_{Carboxylate}$
CH$_4$_sp3 - O$_{NO3}$

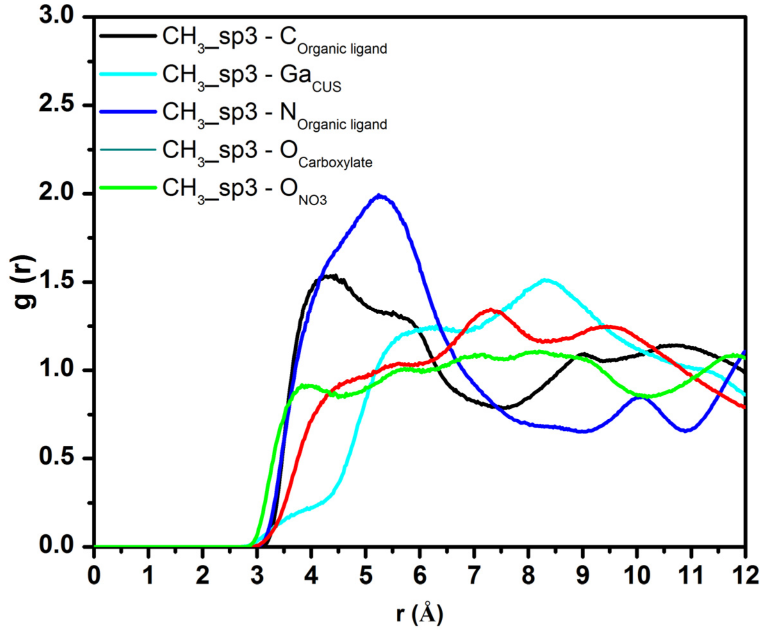
3.0
2.5
2.0
1.5
1.0
0.5
0.0
g (r)
0 1 2 3 4 5 6 7 8 9 10 11 12
r (Å)
CH$_3$_sp3 - C$_{Organic\ ligand}$
CH$_3$_sp3 - Ga$_{CUS}$
CH$_3$_sp3 - N$_{Organic\ ligand}$
CH$_3$_sp3 - O$_{Carboxylate}$
CH$_3$_sp3 - O$_{NO3}$

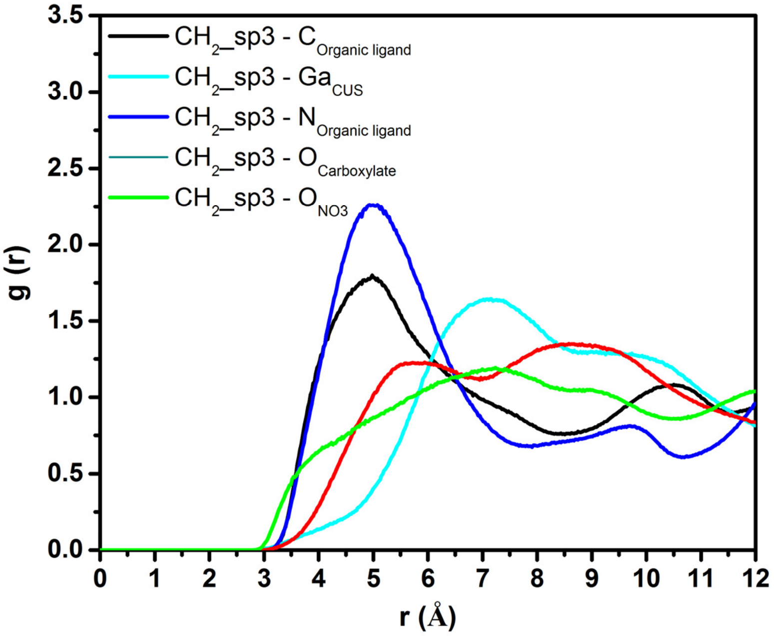

**Figure S19.** Radial distribution functions between both $CH_4$ and *n*-$C_4H_{10}$ and the atoms of the MOF framework: $CH_4$ (a), $CH_3$ (b), and -$CH_2$- (c) centers (organic linker carbon, $C_{Organic\ Linker}$: black, carboxylate oxygen, $O_{Carboxylate}$: red, organic linker nitrogen, $N_{Organic\ Linker}$: blue, nitrate oxygen, $O_{NO3}$: green and CUS Gallium $Ga_{CUS}$: cyan) extracted from the GCMC simulations for a binary mixture (5% *n*-$C_4H_{10}$, 95% $CH_4$) in Ga-**soc**-MOF-1a at 1 bar and 298 K.

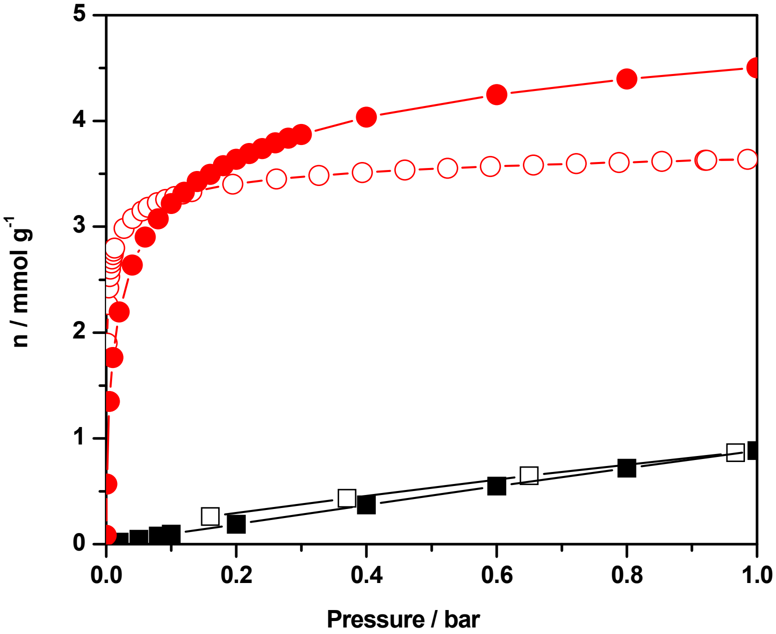

**Figure S20**. Comparison of the single component adsorption isotherms for $CH_4$ (squares) and *n*-$C_4H_{10}$ (circles) at 298 K in Ga-**soc**-MOF-1a: GCMC simulations (full symbols and solid lines) and experiments (empty symbols and dashed lines).

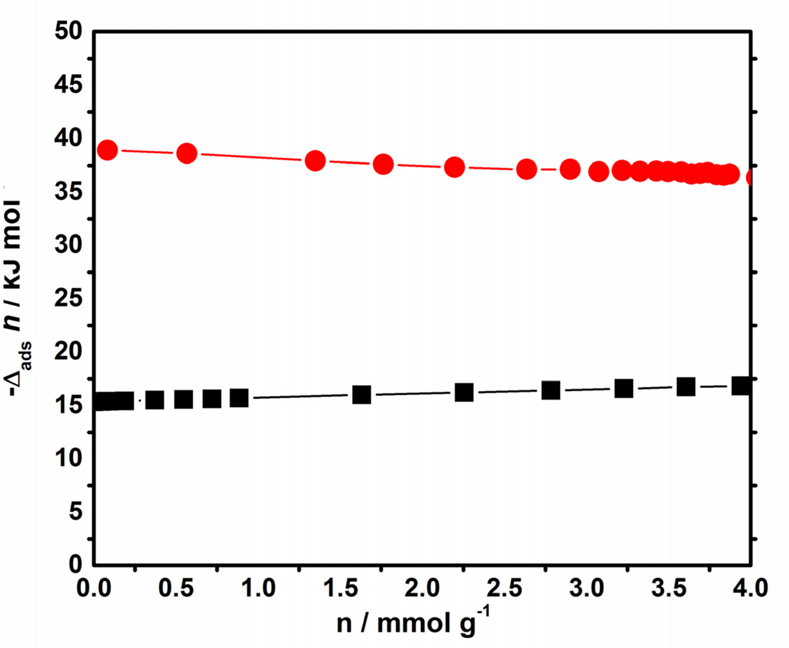

**Figure S21**. Comparison of the single component adsorption isotherms for $CH_4$ (squares) and *n*-$C_4H_{10}$ (circles) at 298 K in Ga-**soc**-MOF-1a: GCMC simulations (full symbols and solid lines) and experiments (empty symbols and dashed lines).

## 5. $H_2S$ Removal performance and stability of soc-MOFs

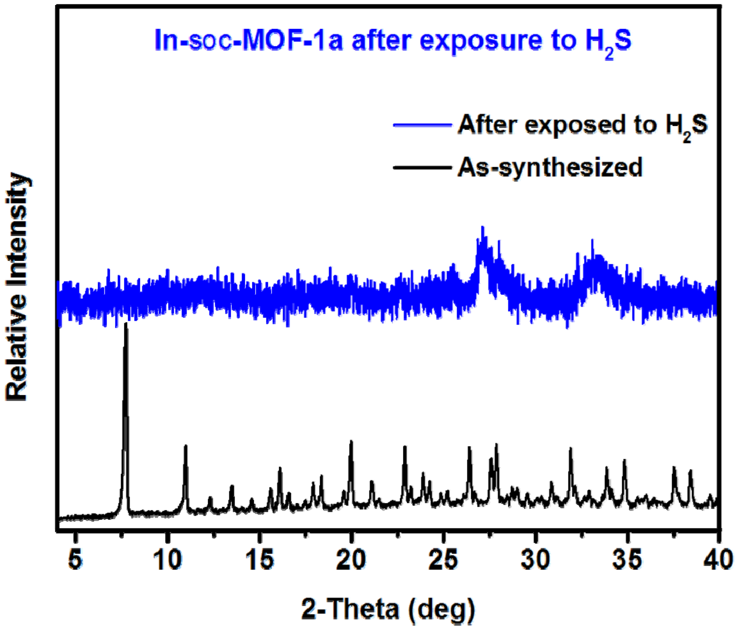

**Figure S22**. PXRD of In-**soc**-MOF-1a after $H_2S$ exposure

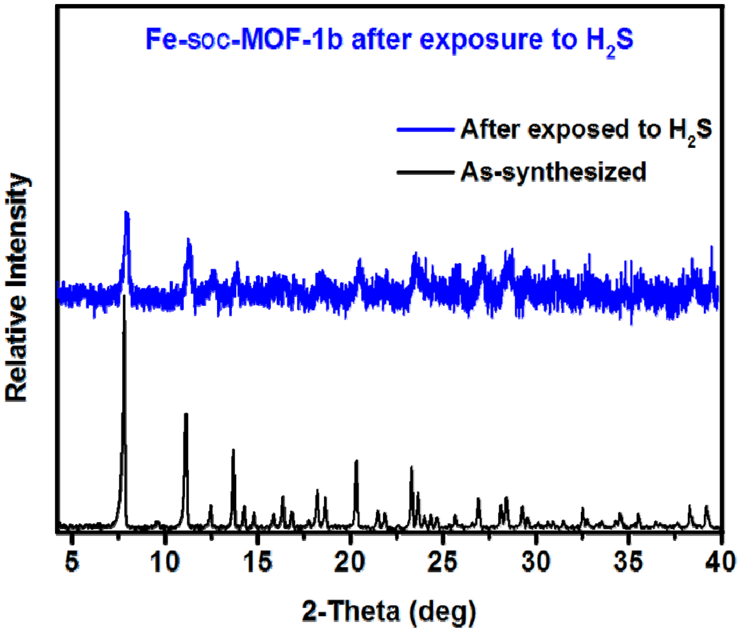

**Figure S23**. PXRD of Fe-**soc**-MOF-1b after $H_2S$ exposure

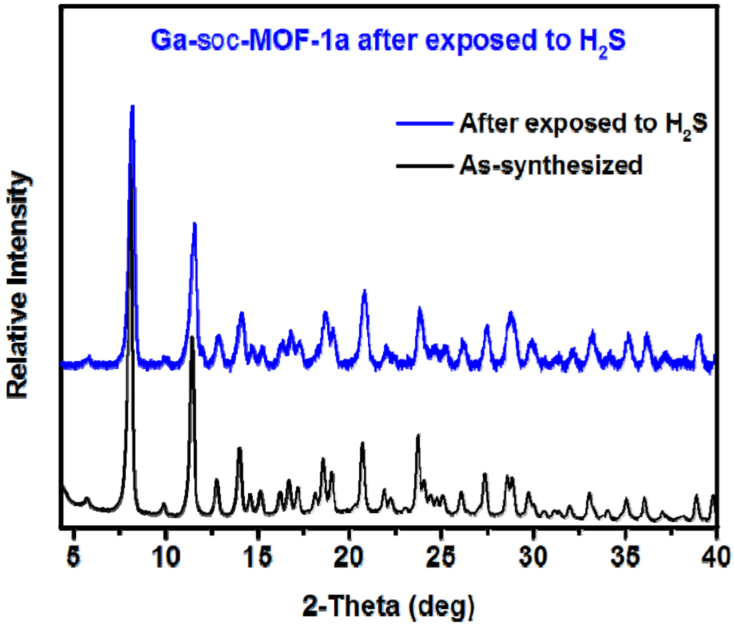

**Figure S24**. PXRD of Ga-**soc**-MOF-1a after $H_2S$ exposure

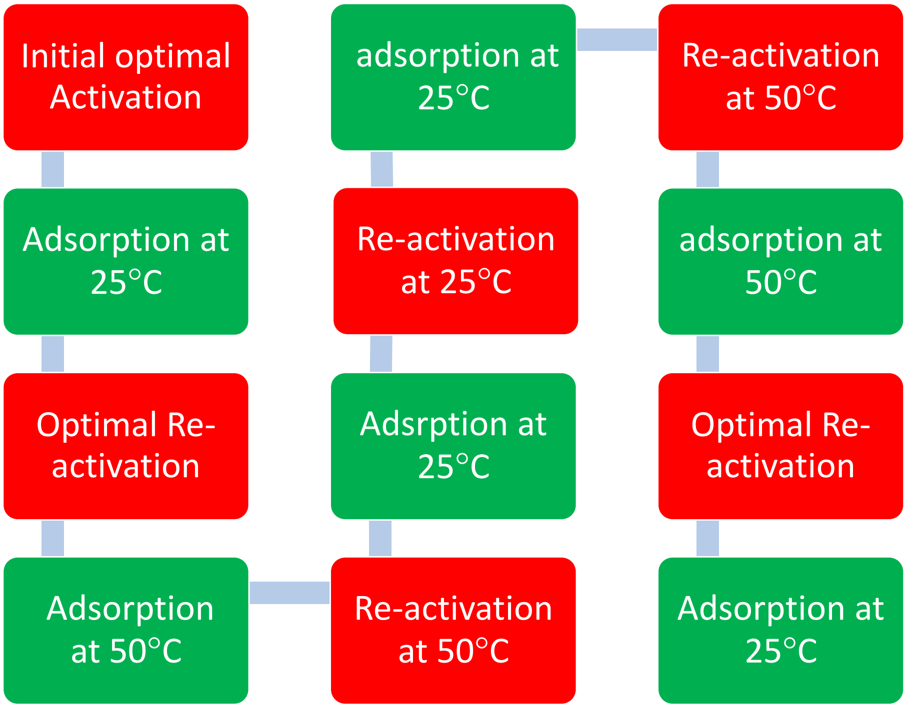

**Figure S25**: Sequence of tests for adsorption column breakthrough studies to evaluate the performances of the materials in temperature swing cyclic (TSR) and vacuum swing regeneration (VSR) modes using $CO_2/H_2S/CH_4$:5/5/90 mixture.

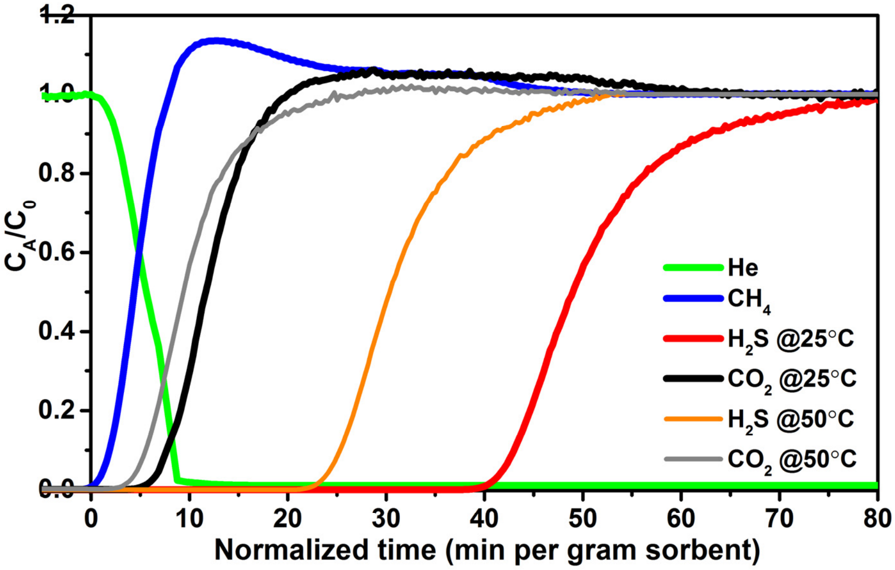

**Figure S26:** Column breakthrough tests of $CO_2/H_2S/CH_4$:5/5/90 with 10 $cm^3$/min flow rate on Ga-**soc**-MOF at 25°C and 50°C (1 bar) respectively using TSR mode (effect of adsorption temperature on the retention time).

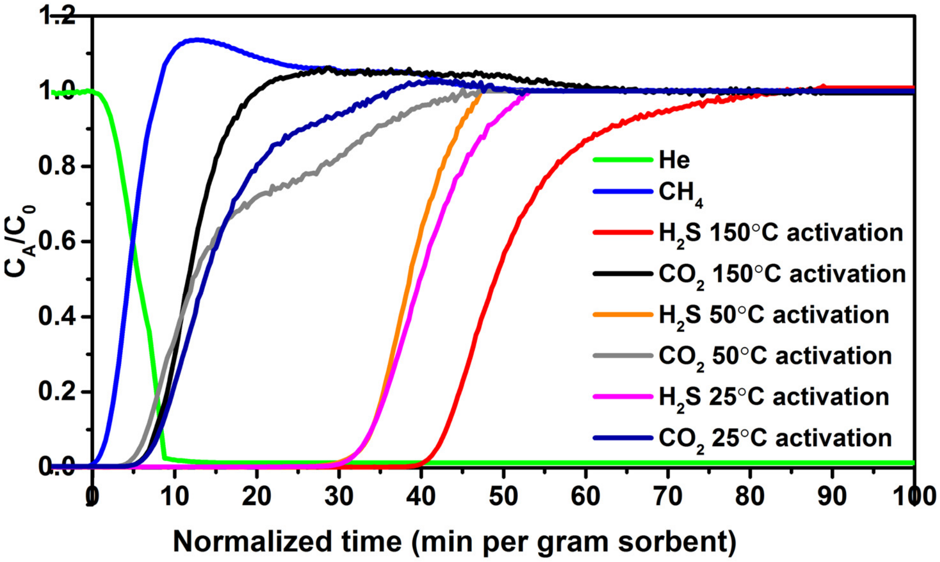

**Figure S27:** Column breakthrough tests of $CO_2/H_2S/CH_4$:5/5/90 with 10 $cm^3$/min flow rate on Ga-**soc**-MOF at 25°C (1 bar) after activation at different temperatures (effect of activation temperature on retention time of different gases).

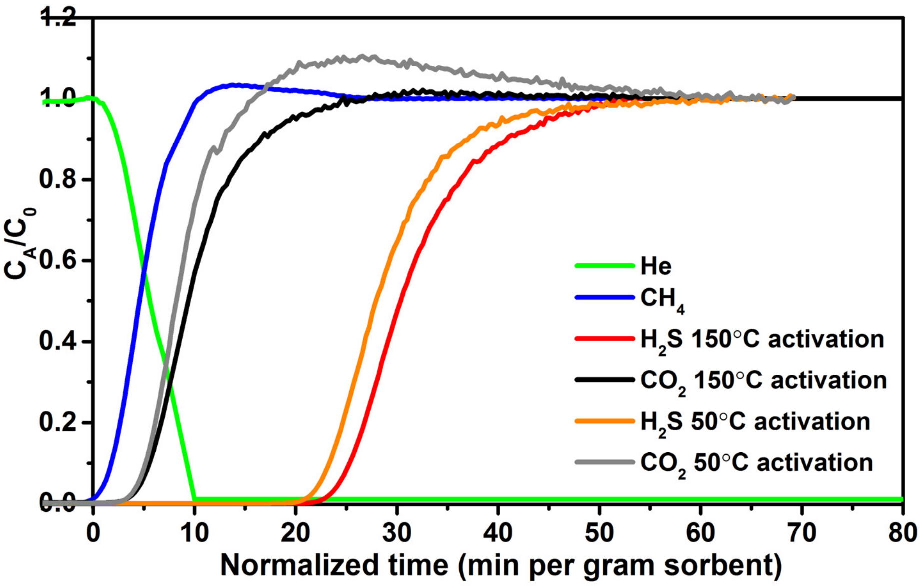

**Figure S28:** Column breakthrough tests of $CO_2/H_2S/CH_4$:5/5/90 with 10 $cm^3$/min flow rate on Ga-**soc**-MOF at 50°C (1 bar) after activation at different temperatures (effect of activation temperature on retention time of different gases).

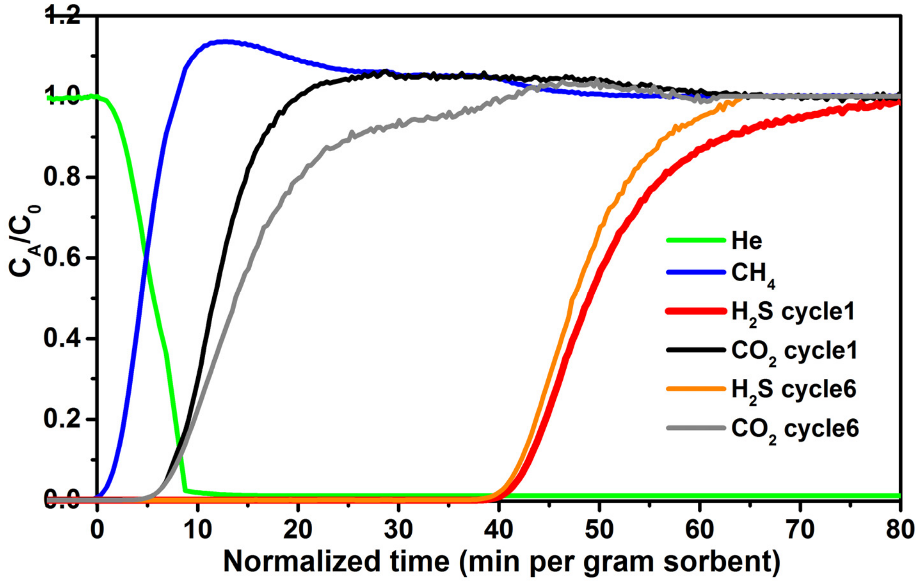

**Figure S29:** Column breakthrough tests of $CO_2/H_2S/CH_4$:5/5/90 with 10 $cm^3$/min flow rate on Ga-**soc**-MOF-1a at 25°C (1 bar) after optimal activation (8 hours under flow of helium at 160°C for cycles 1 and 5) with fresh sample and after five adsorption breakthrough cycles, confirming the recyclability of the material. The conditions for adsorption-desorption cycles for 2, 3 and 4 are reported in Figure S25.

## 6. Characterization of the Aluminum-based soc-MOF (Al-soc-MOF-1d)

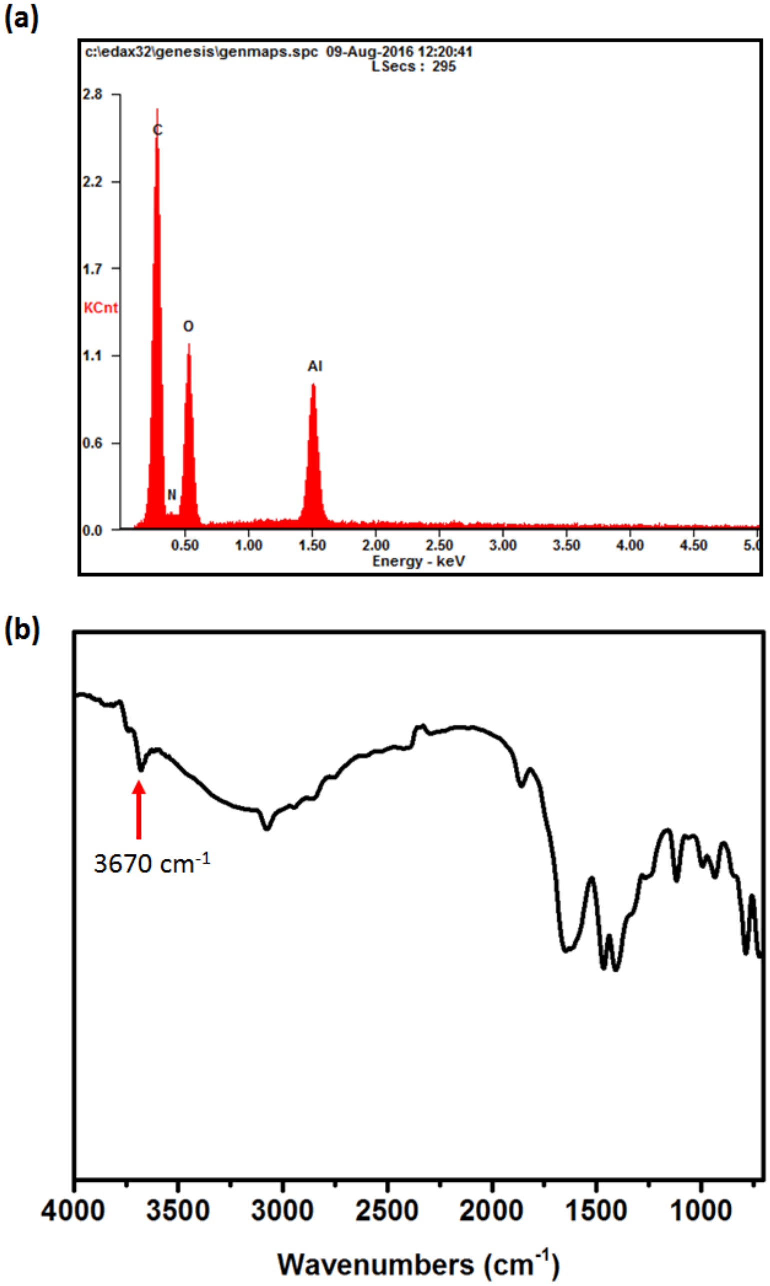

**Figure S30: (a)** EDX data on Al-soc-MOF-1d confirming the absence of chloride. **(b)** In-situ FTIR on dried Al-**soc**-MOF-1d confirming the presence of $OH^-$ as counter ion

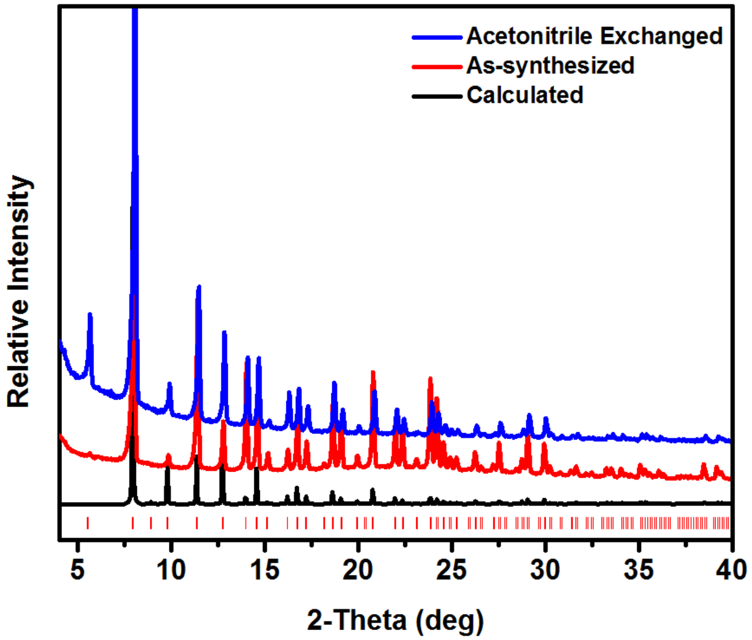

Figure S31: Experimental and calculated PXRD patterns for Al-soc-MOF-1d, indicating the purity of the as-synthesized and acetonitrile exchanged samples.

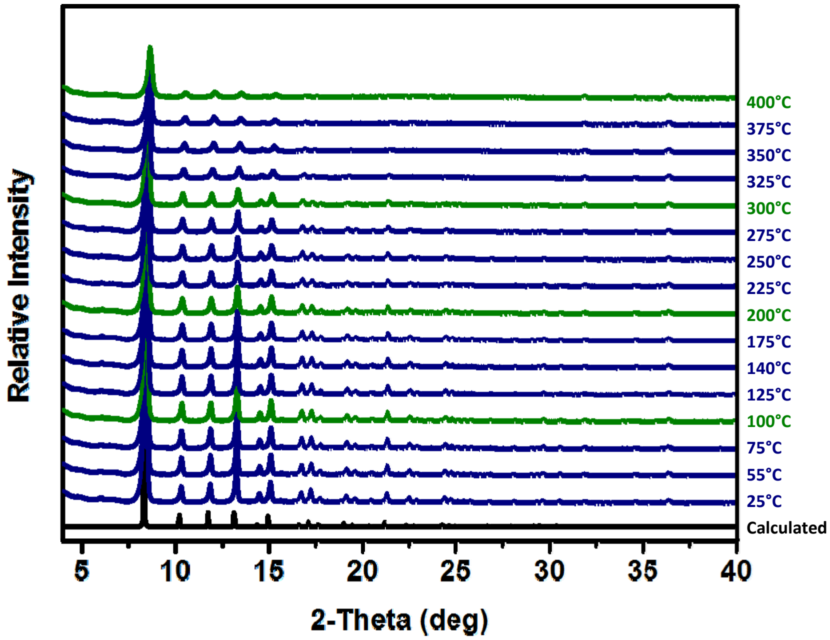

**Figure S32:** Thermal stability of Al-**soc**-MOF-1d

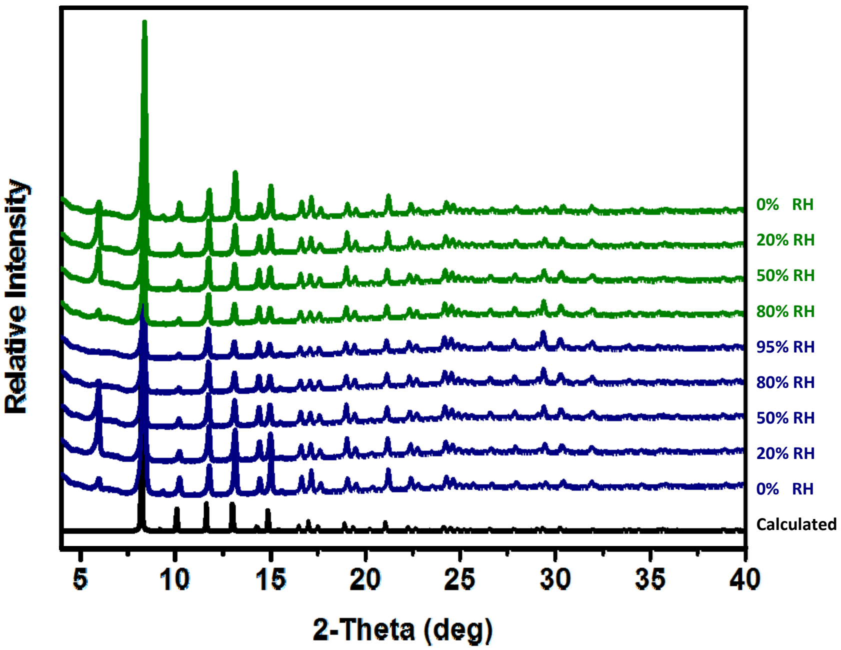

**Figure S33:** Variable humidity PXRD on Al-**soc**-MOF-1d

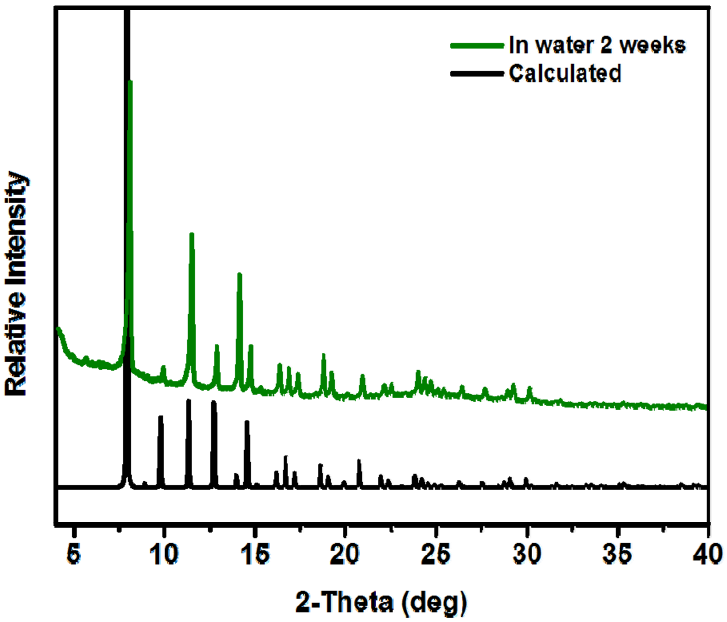

**Figure S34:** PXRD after soaking Al-**soc**-MOF-1d in liquid water for two weeks

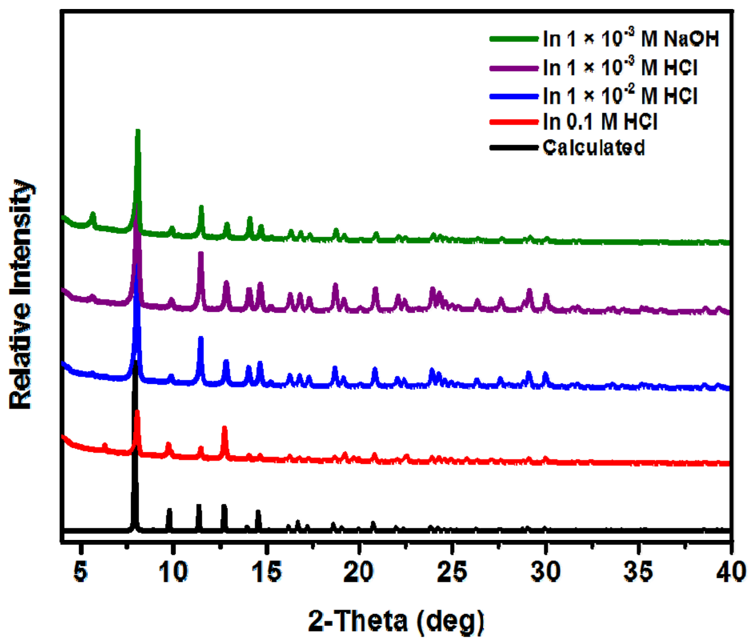

**Figure S35:** PXRD after soaking Al-**soc**-MOF-1d in different pH solutions for 6 days.

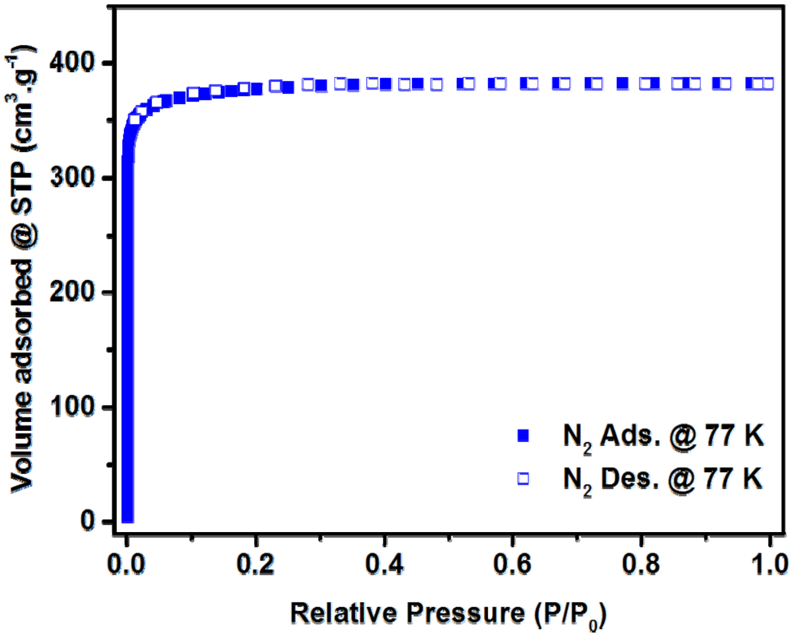

**Figure S36:** $N_2$ adsorption at 77 K on Al-**soc**-MOF-1d

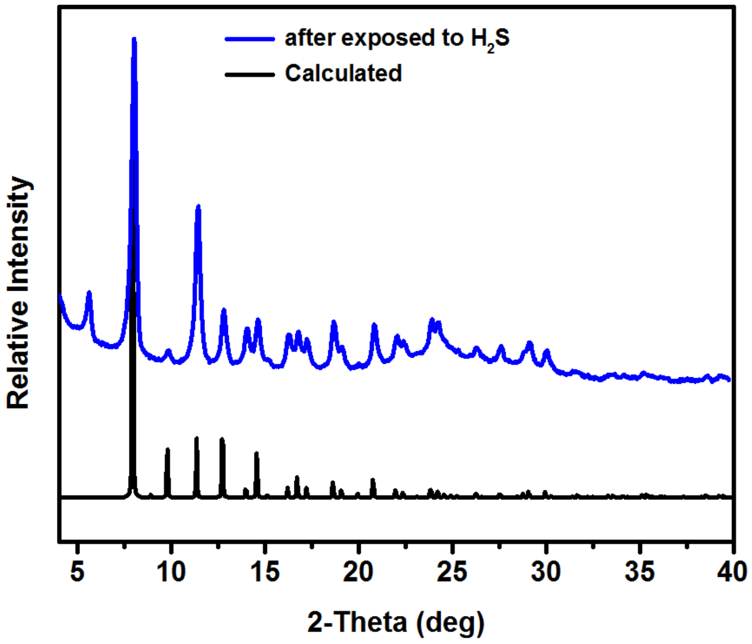

**Figure S37:** PXRD after exposure of Al-**soc**-MOF-1d to $H_2S$

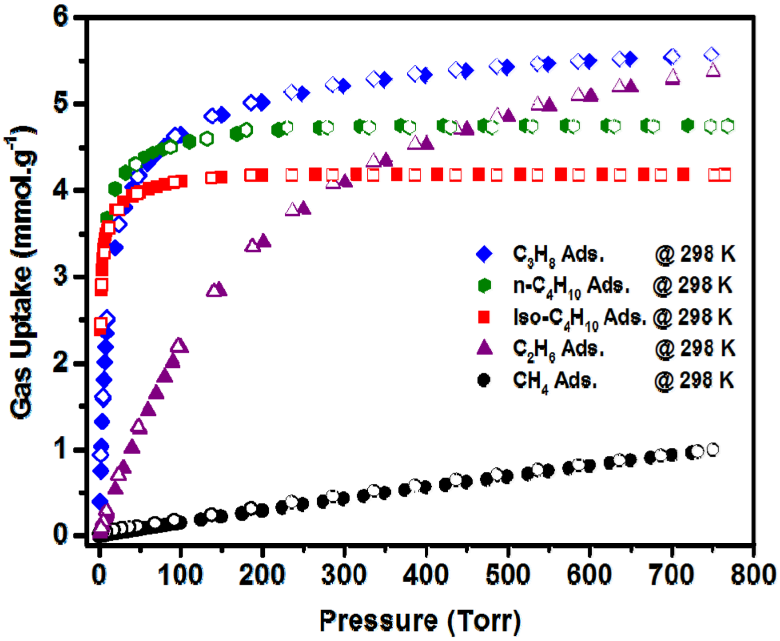

**Figure S38:** Adsorption of $CH_4$, $C_2H_6$, $C_3H_8$, *n*-$C_4H_{10}$ and *iso*-$C_4H_{10}$ on Al-**soc**-MOF-1d

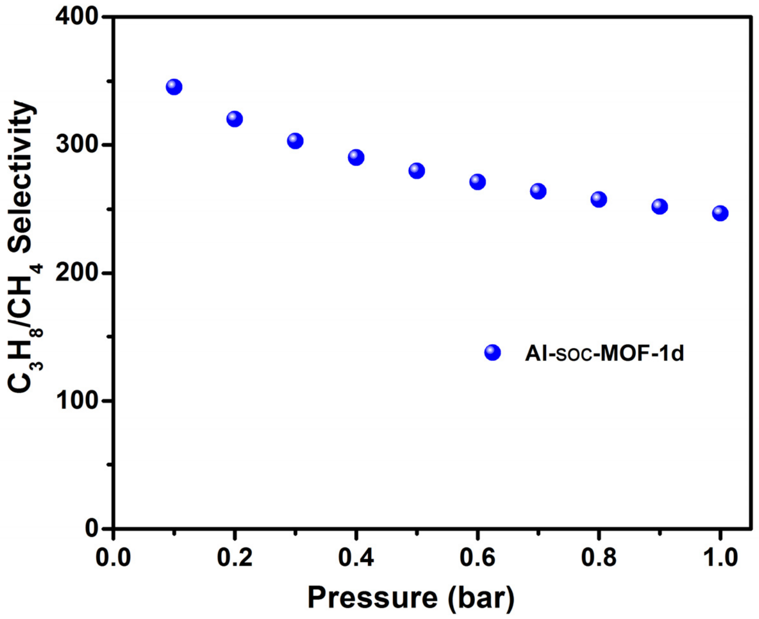

**Figure S39:** $C_3H_8/CH_4$ selectivity using Al-**soc**-MOF-1d predicted using IAST combined with Toth Model.

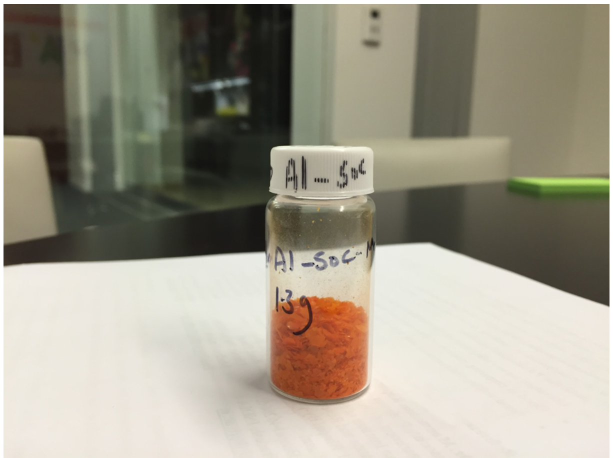

**Figure S40:** Picture of vial containing Al-**soc-**MOF-1d bulk material scaled up to 1 g.

## 7. soc-MOF membrane

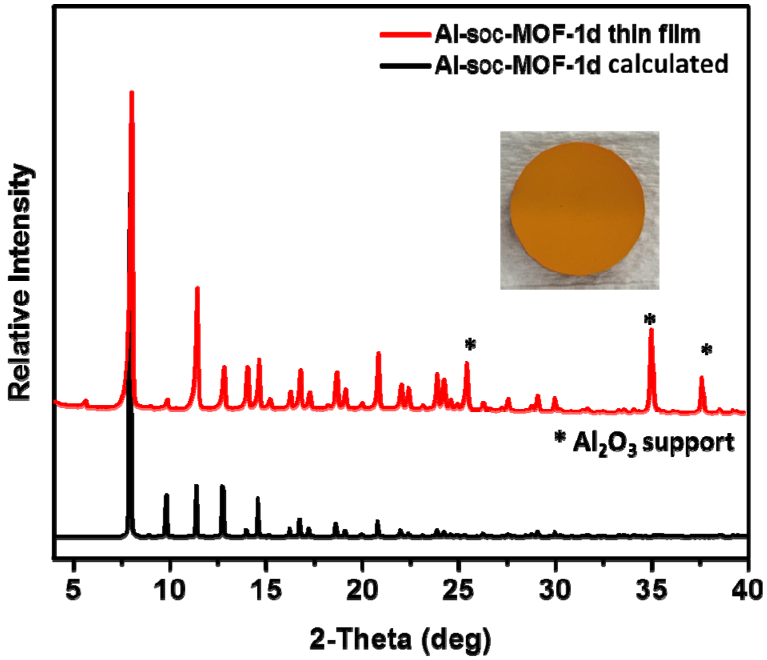

**Figure S41:** Al-**soc**-MOF-1d membrane grown on alumina support and its associated powder X-ray diffraction as compared to the bulk material.

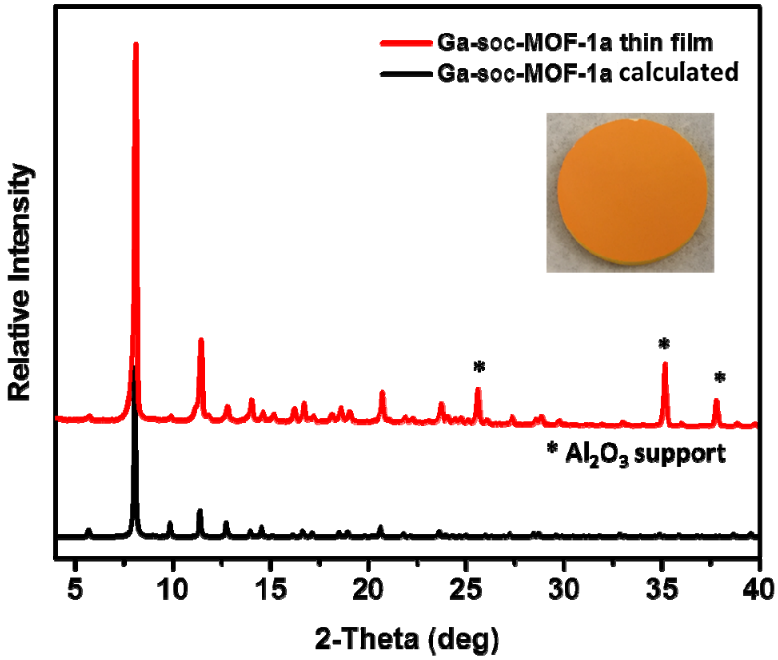

**Figure S42:** Ga-**soc**-MOF-1a membrane grown on alumina support and its associated powder X-ray diffraction as compared to the bulk material

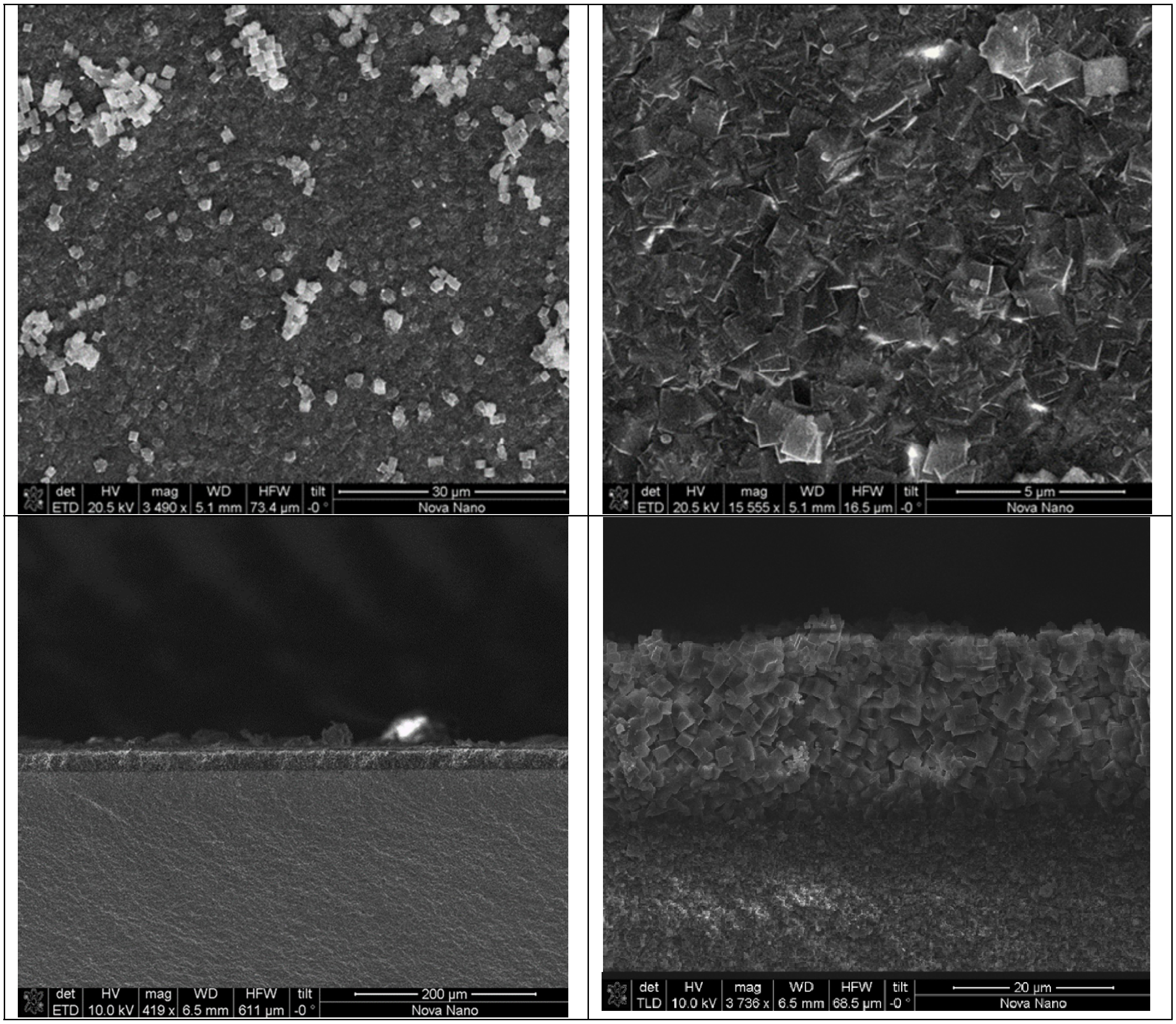

**Figure S43:** (Top) Top-view SEM images of the Ga-**soc**-MOF-1a membranes grown on the alumina support and (down) Cross section image of the membrane.

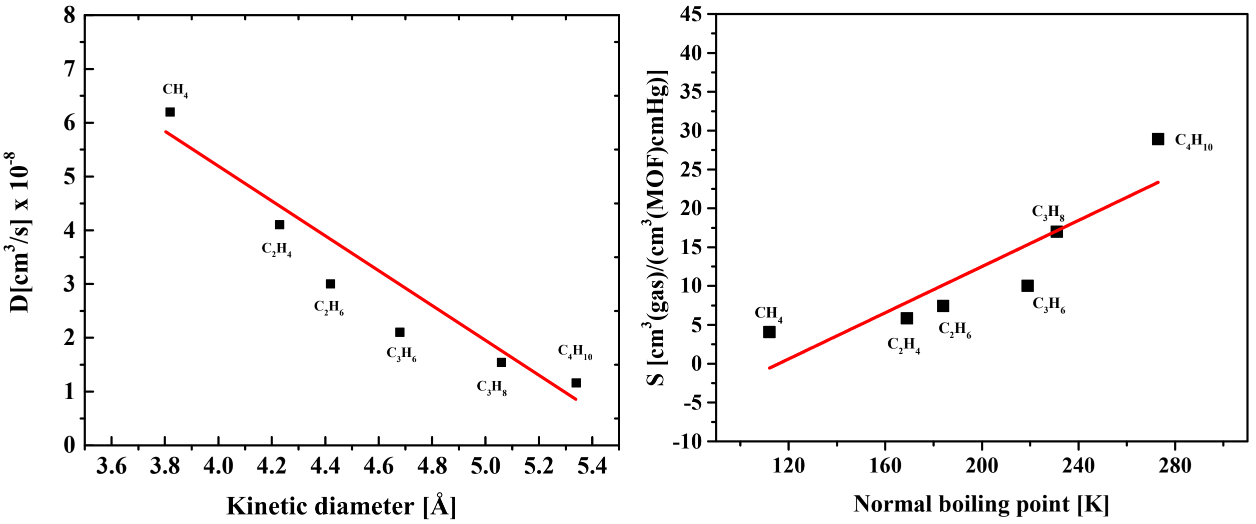

**Figure S44:** (left) Diffusion coefficient vs kinetic Diameter, (right) Adsorption coefficient vs. Normal boiling point for Fe-**soc**-MOF-1a.

**Table S9**: Ideal selectivity for different gas mixtures calculated from single gas permeabilities**.**

| **Gas mixture** | **Ideal selectivity** |
|---|---|
| $H_2/CO_2$ | 4.6 |
| $H_2/N_2$ | 3.8 |
| $CO_2/CH_4$ | 1.8 |
| $C_2H_6/C_2H_4$ | 1.1 |
| $C_3H_8/C_3H_6$ | 1.3 |
| $C_4H_{10}/CH_4$ | 2.2 |

**Table S10**: comparison of $C_3H_8$/ $CH_4$ selectivity of soc-MOF adsorbents as compared to best MOF reported

| **MOF** | **IAST $C_3H_8/CH_4$ selectivity at 1 bar** | **Composition** | **References** |
|---|---|---|---|
| 13X | 158 | 5/95 | Costa E et al, 1991, J.Chem.Eng.Data 36,218 |
| MFM-202a | 90 | 50/50 | Schröder et al. 2016, Chem. Mater. 28, 2331−2340 |
| RE-1,4- NDC-**fcu**-MOFs | 325 | 5/95 | Eddaoudi et al. 2015, *J. Am. Chem. Soc.*, *137* (15),5034–5040 |
| **tbo**-MOF-2 | 140 | 5/95 | Eddaoudi et al. 2014, RSC Adv., 2014, 4, 63855–63859 |
| Ga-**soc**-MOF-1a | 370 | 5/95 | This work |
| In-**soc**-MOF-1c | 500 | 5/95 | This work |
| Fe-**soc**-MOF-1b | 800 | 5/95 | This work |

# 8. References

1. Bonhomme, C.; Gervais, C.; Laurencin, D.; Morris, R. E.; Vimont, A.; Daturi, M.; Horcajada, P.; Serre, C. Chem. Comm., 2013, 49, 7773 – 7775.
2. Inc, B. A. APEX2 (Version 2013.6-2), Bruker AXS Inc: Madison, Wisconsin, USA, 2013.
3. Bruker SAINT-V8.32A, Bruker AXS. Inc: Madison, Wisconsin, USA, 2013.
4. Sheldrick, G. M. SADABS, University of Gottingen, Germany, 1996.
5. J.-R. Li, R. J. Kuppler and H.-C. Zhou, *Chem Soc Rev*, 2009, **38**, 1477-1504.
6. Y. Zhao and D. G. Truhlar, *Theor. Chem. Acc.,* 2008, **120**, 215-241.
7. M. J. Frisch, G. W. Trucks, H. B. Schlegel, G. E. Scuseria, M. A. Robb, J. R. Cheeseman, G. Scalmani, V. Barone, B. Mennucci, G. A. Petersson, H. Nakatsuji, M. Caricato, X. Li, H. P. Hratchian, A. F. Izmaylov, J. Bloino, G. Zheng, J. L. Sonnenberg, M. Hada, M. Ehara, K. Toyota, R. Fukuda, J. Hasegawa, M. Ishida, T. Nakajima, Y. Honda, O. Kitao, H. Nakai, T. Vreven, J. Montgomery, J. A., J. E. Peralta, F. Ogliaro, M. Bearpark, J. J. Heyd, E. Brothers, K. N. Kudin, V. N. Staroverov, R. Kobayashi, J. Normand, K. Raghavachari, A. Rendell, J. C. Burant, S. S. Iyengar, J. Tomasi, M. Cossi, N. Rega, J. M. Millam, M. Klene, J. E. Knox, J. B. Cross, V. Bakken, C. Adamo, J. Jaramillo, R. Gomperts, R. E. Stratmann, O. Yazyev, A. J. Austin, R. Cammi, C. Pomelli, J. W. Ochterski, R. L. Martin, K. Morokuma, V. G. Zakrzewski, G. A. Voth, P. Salvador, J. J. Dannenberg, S. Dapprich, A. D. Daniels, Ö. Farkas, J. B. Foresman, J. V. Ortiz, J. Cioslowski and D. J. Fox, *Gaussian, Inc., Wallingford CT*, 2009.
8. A. K. Rappe, C. J. Casewit, K. S. Colwell, W. A. Goddard and W. M. Skiff, *J. Am. Chem. Soc.*, 1992, **114**, 10024-10035.
9. S. L. Mayo, B. D. Olafson and W. A. Goddard, *J. Phys. Chem.*, 1990, **94**, 8897-8909.
10. M. G. Martin and J. I. Siepmann, *The Journal of Physical Chemistry B*, 1998, **102**, 2569-2577.
11. L.-C. Lin, K. Lee, L. Gagliardi, J. B. Neaton and B. Smit, *J Chem Theory Comput*, 2014, **10**, 1477-1488.